

The nitric oxide formation in anode baking furnace through numerical modeling

Nakate, Prajakta; Lahaye, Domenico; Vuik, Cornelis

DOI

[10.1016/j.ijft.2021.100122](https://doi.org/10.1016/j.ijft.2021.100122)

Publication date

2021

Document Version

Final published version

Published in

International Journal of Thermofluids

Citation (APA)

Nakate, P., Lahaye, D., & Vuik, C. (2021). The nitric oxide formation in anode baking furnace through numerical modeling. *International Journal of Thermofluids*, 12, Article 100122. <https://doi.org/10.1016/j.ijft.2021.100122>

Important note

To cite this publication, please use the final published version (if applicable). Please check the document version above.

Copyright

Other than for strictly personal use, it is not permitted to download, forward or distribute the text or part of it, without the consent of the author(s) and/or copyright holder(s), unless the work is under an open content license such as Creative Commons.

Takedown policy

Please contact us and provide details if you believe this document breaches copyrights. We will remove access to the work immediately and investigate your claim.



The nitric oxide formation in anode baking furnace through numerical modeling

Prajakta Nakate^{a,b,*}, Domenico Lahaye^a, Cornelis Vuik^a

^a Delft University of Technology, The Netherlands

^b Aluminium and Chemie, Rotterdam B.V., The Netherlands

ARTICLE INFO

Keywords:

Thermal NOx formation
Industrial furnace
Diffusion tuning
Eddy dissipation model
P1 approximation model

ABSTRACT

Thermal nitric-oxide (NOx) formation in industrial furnaces due to local overheating is a widely known problem. Various industries made significant investments to reduce thermal NOx by varying the operating conditions and designs of the furnace. It is difficult to find the optimal operating conditions that minimize NOx formation in the furnace by trial and error methods. The high temperature in the furnace complicates performing experiments in the furnace. Numerical modeling can provide significant information in such cases. Therefore, the objective of this paper is to obtain a numerical model of the furnace in such a way that the operating conditions can be varied and examined.

In this paper, a three-dimensional steady-state finite element model for the anode baking industrial furnace is discussed. The COMSOL Multiphysics software is used for modeling the non-premixed turbulent combustion and the conjugate heat transfer to the insulation lining. The cfMesh software is used for obtaining the mesh. The results show that the simulated temperature agrees well with the measured data from our industrial partner in regions distant from the flames. The analysis shows that by decreasing the fuel mass flow rate and increasing the fuel pipe diameter by 45%, the peak in thermal NOx ppm generated in the furnace decreases by 42%. The model is limited by the use of a single-step chemistry mechanism with an eddy dissipation combustion model and a simplified approach for radiation, such as the P1 approximation model. The model can be further improved by considering a detailed chemistry mechanism model for combustion and a discrete ordinate model for radiation.

1. Introduction

Industrial emissions are discussed worldwide due to its significant impact on climate change. Among the various hazardous gases emitted, reducing nitrogen oxides (NOx) have been a priority for many industries. The NOx formation can be attributed to four prime processes. The thermal NOx, which is the largest contributor, is formed from the atmospheric nitrogen at the temperatures higher than 1300 °C. The other three processes are prompt NOx, fuel NOx formed by the nitrogen containing fuels and NOx formation in lean mixtures at elevated pressures via intermediate formation of N₂O [1]. The study of high temperature regions is required since the majority of NOx formation in industries is by thermal process. Studying these temperatures by a traditional trial and error approach is difficult. These methods can also lead to longer times and may require higher resources. Moreover, sometimes dealing with high temperatures in the furnace for the experiment is impossible. Therefore, learning from the numerical model of these processes is preferred.

NOx emissions from industrial furnaces have been widely discussed [2]. Anode baking process is one example in which the thermal NOx is formed due to high temperatures. Anode baking process has significant contribution in Aluminum industries [3]. The heat required for the baking process is produced by the combustion of natural gas in a furnace. The resulting temperature in the furnace is well above 1300 °C. Therefore, the thermal NOx produced in the furnace is significant. In this work, the anode baking furnace of the company named Aluchemie in Rotterdam, Netherlands is studied to reduce the NOx from the furnace. The various physics involved in the process are turbulent flow, combustion, radiation and conjugate heat transfer. The multi-physics modeling can be carried out to analyze the temperature in the furnace. This can provide significant information on the generation of NOx. The anode baking process practiced in Aluchemie furnace is described in the previous paper [4] that describes the aerodynamics in the furnace. The study on NOx emissions continues in this paper.

* Corresponding author at: Delft University of Technology, The Netherlands.
E-mail address: p.a.nakate@tudelft.nl (P. Nakate).

<https://doi.org/10.1016/j.ijtf.2021.100122>

Received 15 June 2021; Received in revised form 28 September 2021; Accepted 13 October 2021

Available online 28 October 2021

2666-2027/© 2021 The Authors. Published by Elsevier Ltd. This is an open access article under the CC BY license (<http://creativecommons.org/licenses/by/4.0/>).

Nomenclature

ρ	Density, kg/m ³
\mathbf{u}	Velocity, m/s
p	Reference press, Pa
μ	Dynamics viscosity, kg/m s
μ_T	Turbulent viscosity, kg/m s
k	Turbulent kinetic energy, m ² /s ²
ϵ	Turbulent dissipation rate, m ² /s ³
I_T	Turbulent intensity, %
L_T	Turbulent length scale, m
w	Mass fraction
D^f	Fick's diffusion coefficient, m ² /s
M_n	Mean molar mass, kg/mol
c_{art}	Artificial diffusion coefficient, m ² /s
δ_{id}	Tuning parameter
h	Mesh size, m
β	Convective velocity vector, m/s
ν	Stoichiometric coefficient
τ_T	Turbulent time scale, s
C_p	Specific heat capacity, J/kg °C
T	Temperature, °C
q	Heat flux, J/m ² s
Q	Heat source, J/m ³
k	Thermal conductivity, W/m °C
Q_r	Radiative heat source, J/m ³
κ	Absorption coefficient, 1/m
I_b	Black body radiation, W/m ²
G	Incident radiation, W/m ²
ξ	Emissivity

Subscripts

i	Chemical species
r	Reactant
MV	Mean value
$solid$	Solid domain
p	Product
ED	Eddy dissipation
$fluid$	Fluid domain
$P1$	P1 approximation model

Superscripts

for	Forward
rev	Reverse

Therefore, as detailed in the previous paper, the heating section of the furnace is important for the study of NOx formation.

The modeling of the anode baking process is used since 1980's. The earlier developed models lacked the complexity due to limited resources and knowledge [5]. However, they provide strong foundation to the models developed in the later stage. The modeling of anode baking process improved significantly in the last few decades starting from 2D models to more sophisticated 3D models. The focus of the modeling has been on the optimized furnace design, increasing the energy efficiency and decreasing the wall deformation [6–11]. Moreover, there have been studies to propose comparisons between various models for the turbulent flow, combustion and radiation [12,13]. These models help to establish the state-of-the-art models. The NOx formation in the anode baking furnace started gaining interest since last few years. The recent models developed by Tajik et al. [14] examines the effect of

inlet oxygen concentration, inlet oxygen temperature, equivalence ratio and thermal properties of refractory walls on the NOx formation. The study suggests a significant impact on NOx by changing inlet oxygen concentration and temperature. The thermal NOx formation highly depends on the maximum temperature in the furnace. The temperature depends on the other operating conditions related to the fuel inlet that governs the mixing phenomena of the two streams. Studying the mixing behavior of the two streams with respect to the NOx formation are still lacking.

The problem statement is defined as the limitation in understanding of NOx generation in the anode baking furnace with respect to fuel flow conditions. The objective of this paper is to provide insights on the NOx formation with respect to the operating conditions, such as fuel mass flow rate and fuel pipe diameter. The variations in these operating conditions result in different flow dynamics in the furnace [15]. The change in the flow dynamics affects the mixing patterns of the fuel and air streams.

In the first part of the paper, the test case model of the existing fuel mass flow rate and fuel pipe diameter is studied. The tuning of the diffusion parameter is carried out by comparing with measured values. The requirement of tuning diffusion in the model equation is discussed. The effect of fuel mass flow rate and fuel pipe diameter on NOx generation are studied. The higher mass flow rate results in higher turbulent viscosity ratio that further increases the NOx formation due to higher temperature in the furnace. Furthermore, the effect of the increasing fuel pipe diameter decreases the turbulent scale thereby lowering the temperature. Therefore, increasing the fuel pipe diameter decreases the NOx in the furnace.

2. Methodology

A three dimensional steady-state numerical model is developed using COMSOL Multiphysics software. The software is based on the finite element solver. The turbulent flow is modeled by the RANS equation. The Reynolds stresses are closed by using the standard $k-\epsilon$ model. The combustion and radiation are modeled using eddy dissipation and P1 approximation model. To model the heat flux conducted to the solid domain, a brick layer is added to the model. The temperatures measured in the furnace are provided as boundary condition at the brick layer that is not in contact with the gas domain. The NOx is computed in the post processing stage using a Zeldovich mechanism.

2.1. Geometry and mesh

The NOx generation in the anode baking furnace occurs in the heating section. In this study, the focus is on modeling the NOx generated in the anode baking furnace. This allows us to restrict to a heating section of the furnace for the model geometry. In order to account for the heat flux going to the anodes, a brick layer is added along the flue domain as shown in Fig. 1. Aluchemie has measured the temperatures at the brick sides using several thermocouples. As the focus in this study is on NOx generation, the interest lies in the temperature distribution in the flue domain. By taking the boundary conditions as the measured temperatures on the brick layer, the heat flux leaving the flue domain can be modeled accurately. Therefore, the model is simplified and restricted to a flue gas domain and the solid brick layer. The approximate dimensions in the XY plane are as shown in Fig. 1. The symmetry is assumed at the flue domain side to reduce the computational time. The dimensions of the model comply with the Aluchemie furnace. The depth of the fluid domain and the brick layer domain in the Z direction are 0.27 m and 0.11 m, respectively. The details of the internal geometry of the fluid domain is elaborated in our previous paper [4] in which the aerodynamics in the flue domain of the furnace is studied. As shown in the figure, the air enters the fluid domain from three inlets whereas there are two fuel inlets at the top. The air and fuel streams are mixed in a cross flow manner.

Table 1
Details of the meshes of two geometries with different fuel pipe diameter.

Diameter of fuel pipe [mm]	Number of elements	Size of elements in refinement zone [mm]	Quality of mesh
9	892784	3	0.89
13	1352854	3	0.84

Aluchemie has measured NOx emissions by varying the nozzle diameters of the burners. In this paper, the burner is simplified to a simple pipe with length 0.11 m. The two diameter values 9 mm and 13 mm of the pipes are considered based on the nozzle diameters of the actual burners. The remaining geometry of the model for the two studies remains the same.

The meshing of the geometries with two diameters of the fuel pipes are carried out with the cfMesh software. In our previous paper, the analysis of different meshing techniques are discussed [4]. The less diffusive Cartesian mesh for the complex geometry of the anode baking furnace can be obtained using cfMesh software. The region under the fuel outlet is refined further for better resolution of the flow in that region. This region is particularly of interest with respect to NOx generation. Fig. 2 shows the meshes of the geometries with the two diameters. It can be observed that the region of the jet development is refined in the same manner for both geometries. The difference is only with respect to the diameter of the fuel pipe. Table 1 provides the details of the two meshes.

The quality of the mesh is measured by the skewness parameter. Obtaining a mesh of similar mesh quality for two diameter of fuel pipes is difficult with the default mesher of COMSOL Multiphysics. Fig. 3 shows the mesh quality histograms in terms of skewness for different diameters of fuel pipe. It can be observed that in some regions of the 13 mm diameter of fuel pipe there are more elements that are of low quality as compared to the 9 mm diameter. However, the overall histogram quality is comparable. cfMesh software provides control over the size of elements in the region of interest and therefore, obtaining meshes with the external software is preferred.

3. Model equations

3.1. Turbulent flow model

The turbulent flow is modeled using Reynolds average Navier–Stokes (RANS) equation as presented in Eq. (1).

$$\rho(\mathbf{u} \cdot \nabla)\mathbf{u} = \nabla \cdot [-p\mathbf{I} + \mathbf{K}], \quad (1)$$

The term \mathbf{K} is defined by Eq. (2).

$$\mathbf{K} = (\mu + \mu_t)(\nabla\mathbf{u} + (\nabla\mathbf{u})^T) - \frac{2}{3}(\mu + \mu_t)(\nabla \cdot \mathbf{u})\mathbf{I} - \frac{2}{3}\rho k\mathbf{I}, \quad (2)$$

The standard $k - \epsilon$ model is used for closing the Reynolds stresses from the RANS equation. The model is the two equation turbulent model defined by the transport equation of turbulent kinetic energy and turbulent dissipation rate as shown in Eqs. (3) and (4), respectively.

$$\rho(\mathbf{u} \cdot \nabla)k = \nabla \cdot [(\mu + \frac{\mu_t}{\sigma_k})\nabla k] + P_k - \rho\epsilon \quad (3)$$

$$\rho(\mathbf{u} \cdot \nabla)\epsilon = \nabla \cdot [(\mu + \frac{\mu_t}{\sigma_\epsilon})\nabla\epsilon] + C_{\epsilon 1}\frac{\epsilon}{k}P_k - C_{\epsilon 2}\rho\frac{\epsilon^2}{k}. \quad (4)$$

The production term P_k is as presented in Eq. (5).

$$P_k = \mu_T(\nabla\mathbf{u} : (\nabla\mathbf{u} + (\nabla\mathbf{u})^T)) - \frac{2}{3}(\nabla \cdot \mathbf{u})^2 - \frac{2}{3}\rho k\nabla \cdot \mathbf{u} \quad (5)$$

The definition of turbulent viscosity μ_T with the standard $k - \epsilon$ model is given in Eq. (6).

$$\mu_T = \rho C_\mu \frac{k^2}{\epsilon} \quad (6)$$

Table 2
Values of the constants for standard $k - \epsilon$ model.

Constant	Value
C_μ	0.09
$C_{\epsilon 1}$	1.44
$C_{\epsilon 2}$	1.92
σ_k	1.00
σ_ϵ	1.30

The values of the constant parameters for the Eqs. (3) and (4) are given in Table 2.

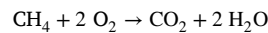
The boundary conditions for the turbulent kinetic energy and turbulent dissipation rate are defined in terms of turbulent length scale and turbulent intensity. These definitions are as presented in Eqs. (7) and (8), respectively.

$$k = \frac{3}{2}(U_{ref} I_T)^2 \quad (7)$$

$$\epsilon = C_\mu^{(3/4)} \frac{k^{(3/2)}}{L_T}. \quad (8)$$

3.2. Eddy dissipation combustion model

Methane is used as fuel in the anode baking process. A simplified one step combustion mechanism of methane is used to quantify chemical species. The reaction is as follows.



The transport equation for each of the species is given by Eqs. (9) and (10).

$$\nabla \cdot \mathbf{j}_i + \rho(\mathbf{u} \cdot \nabla)w_i = R_i \quad (9)$$

$$\mathbf{j}_i = -(\rho D_i^f \nabla w_i + \rho w_i D_i^f \frac{\nabla M_n}{M_n}) \quad (10)$$

The isotropic diffusion can be added to the diffusion coefficient from Eq. (10). This additional diffusion can be varied using a tuning parameter δ_{id} from Eq. (11). In a later section, the effect of variation of this tuning parameter is studied.

$$c_{art} = \delta_{id} h \|\beta\| \quad (11)$$

The reaction term from Eq. (9) is modeled using the eddy dissipation model. The regularization is implemented to ensure that the reactant is consumed only when its mass fraction value is higher than zero. Moreover, the mass fraction of the product is restricted to take the maximum value of 1. The eddy dissipation model equations are given by Eqs. (12) to (16).

$$R_i = \frac{1}{2} \frac{R_i^c - |R_i^c|}{\max(w_i, w_i^{dl})} \max(w_i, 0) + \frac{1}{2} \frac{R_i^c + |R_i^c|}{\max(1 - w_i, w_i^{dl})} \max(1 - w_i, 0) \quad (12)$$

$$R_i^c = v_i M_i [\min(r_{MV,i}^{for}, r_{ED,i}^{for}) - \min(r_{MV,i}^{rev}, r_{ED,i}^{rev})] \quad (13)$$

$$r_{MV,i}^{for} = k^{for} \prod_r \left(\frac{\rho w_r}{M_r}\right)^{-v_{i,r}}, \quad r_{MV,i}^{rev} = k^{rev} \prod_p \left(\frac{\rho w_p}{M_p}\right)^{-v_{i,p}} \quad (14)$$

$$r_{ED,i}^{for} = \frac{\alpha\epsilon}{k} \rho \min[\min(\frac{w_r}{v_r M_r}), \beta \sum_p (\frac{w_p}{v_p M_p})] \quad (15)$$

$$r_{ED,i}^{rev} = \frac{\alpha\epsilon}{k} \rho \min[\min(\frac{w_p}{v_p M_p}), \beta \sum_r (\frac{w_r}{v_r M_r})] \quad (16)$$

The default values of $\alpha = 4$ and $\beta = 0.5$ are used. The turbulent time scale determines the mixing intensity of the fuel and oxidizer streams. The Dirichlet boundary conditions are specified for all chemical species transport equations.

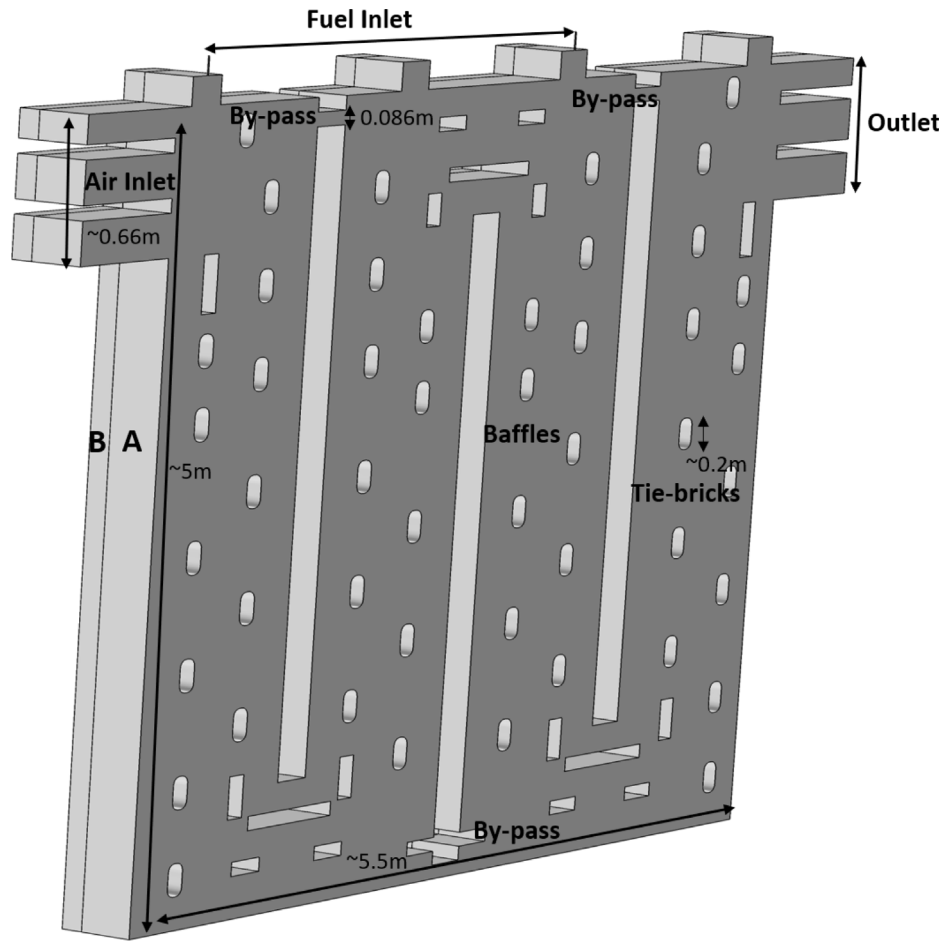


Fig. 1. The 3D geometry of the heating section of anode baking furnace with fluid and solid domain. Domain A is the fluid domain with gaseous interactions and domain B is the refractory brick layer.

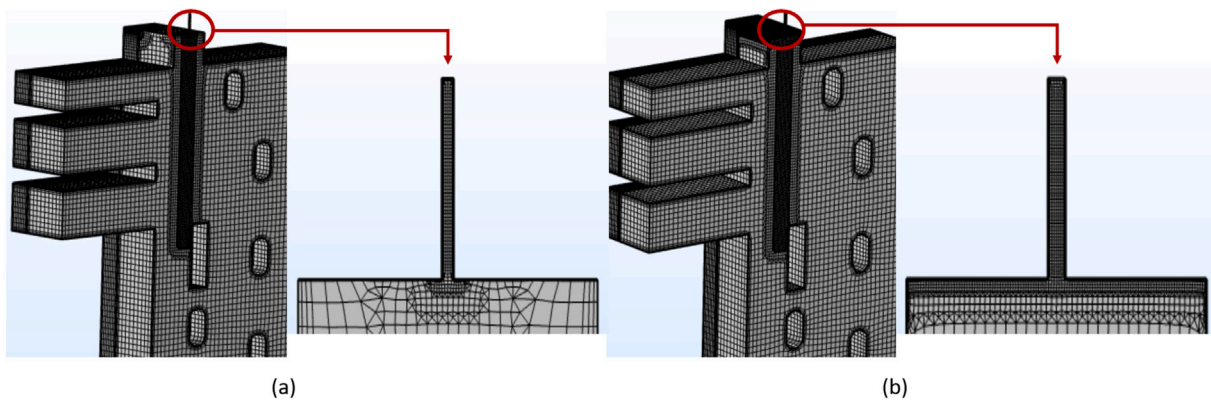


Fig. 2. Comparison of the meshes of geometries with fuel pipe diameters (a) 9 mm and (b) 13 mm. Two meshes of two models differ only at the attachment of fuel pipe to the furnace.

3.3. Energy equation coupled with radiation and conjugate heat transfer

The radiation [16] and conjugate heat transfer [17] are two main modes of heat transfer in anode baking furnace. The energy transport equation for the gas domain in which the combustion process of methane occurs is presented by Eq. (17). The specific heat capacity of gases, namely, CH₄, O₂, CO₂, H₂O and, N₂ are defined by a temperature dependent analytical function. The parameters specific to a certain gas are obtained from NIST database. The specific heat capacity for the mixture of gases is then calculated considering the contribution of each

of the gas.

$$\rho C_p \mathbf{u} \cdot \nabla T + \nabla \cdot \mathbf{q} = Q \tag{17}$$

The combustion of methane translates into the generation of heat energy. This acts as a heat source term, Q , in the energy transport equation solved for the gas domain. The heat energy generated from the combustion process is computed based on the heat of the formation of each of the chemical species and the stoichiometric coefficient of the single step combustion of methane. The heat flux, q , is given by

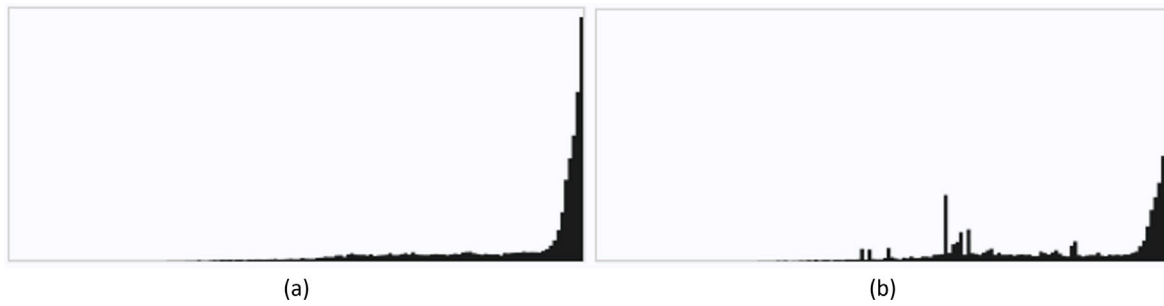


Fig. 3. Histogram of the skewness of the cell in the mesh for the geometry with fuel pipe diameter equal to (a) 9 mm and (b) 13 mm. Meshes of comparable quality can be obtained using the cfMesh software.

Fourier's law as given in Eq. (19).

$$\mathbf{q} = -k_{fluid} \nabla T \quad (18)$$

The heat generated in the gas domain is conducted through walls to anodes. In this model, a single brick layer is considered so as to account for the heat flux conducting to a combined solid phase.

$$\mathbf{q} = -k_{solid} \nabla T \quad (19)$$

The radiation in the gas domain is accounted by the radiative source term as presented in Eq. (20). The incident radiation, G , is computed by the P1 approximation model as defined by Eq. (21).

$$Q_r = \kappa(G - 4\pi I_b) \quad (20)$$

$$\nabla \cdot (D_{P1} \nabla G) - \kappa(G - 4\pi I_b) \quad (21)$$

The diffusion coefficient of the P1 approximation is defined based on the absorption and scattering coefficient as presented in Eq. (22). The scattering is neglected by assigning value zero to σ_s .

$$D_{P1} = \frac{1}{3(\kappa + \sigma_s)} \quad (22)$$

The radiative flux through boundaries is defined by Eqs. (23) and (24). The emissivity of the walls is defined by the temperature dependent interpolation function based on the data provided by the brick manufacturer.

$$-\mathbf{n} \cdot (-D_{P1} \nabla G) = -q_{r,net} \quad (23)$$

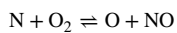
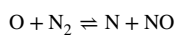
$$q_{r,net} = \frac{\xi}{2(2 - \xi)} (4\pi I_{b,w}(T) - G) \quad (24)$$

3.4. NOx calculations by Zeldovich mechanism

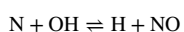
The NOx is calculated in the post processing stage by solving stabilized convection diffusion equation as given by Eq. (25).

$$\nabla \cdot (\rho \mathbf{u} w_{NO}) = \nabla \cdot (\rho D^f \nabla w_{NO}) + S_{NO} \quad (25)$$

The thermal NOx source term from Eq. (25) is modeled in the post processing stage using the extended Zeldovich mechanism. Following two major reactions govern the formation of thermal NOx.



Whereas, the third reaction is significant only in the fuel rich mixtures.



The rate constants for these reactions are provided in Table 3.

Table 3

Rate constants of the Zeldovich mechanism reactions.

Rate constant	Value [m ³ /mol-s]
$k_{f,1}$	$1.8 \times 10^8 e^{-38370/T}$
$k_{f,2}$	$1.8 \times 10^4 e^{-4680/T}$
$k_{f,3}$	$7.1 \times 10^7 e^{-450/T}$
$k_{r,1}$	$3.8 \times 10^7 e^{-425/T}$
$k_{r,2}$	$3.81 \times 10^3 e^{-20820/T}$
$k_{r,3}$	$1.7 \times 10^8 e^{-24560/T}$

The net rate of formation of NO based on the listed reactions and quasi-steady state assumption for the concentration of N radical is given by Eq. (26).

$$\frac{d[\text{NO}]}{dt} = 2k_{f,1}[\text{O}][\text{N}_2] \frac{(1 - \frac{k_{r,1}k_{r,2}[\text{NO}]^2}{k_{f,1}[\text{N}_2]k_{f,2}[\text{O}_2]})}{(1 + \frac{k_{r,1}[\text{NO}]}{k_{f,2}[\text{O}_2] + k_{f,3}[\text{OH}]})} \quad (26)$$

The O radical concentration is calculated based on the equilibrium approach and is given by Eq. (27).

$$[\text{O}] = 3.97 \times 10^5 T^{-1/2} [\text{O}_2]^{1/2} e^{-31090/T} \quad (27)$$

The source term from Eq. (25) is calculated using Eq. (28).

$$S_{NO} = M_{NO} \frac{d[\text{NO}]}{dt} \quad (28)$$

The validation of the model obtained by using the above mentioned numerical equations is carried out by comparing model values with that of the measured values in the furnace. The validation is further elaborated in Section 4.1.

3.5. Finite element discretization and solver

In this paper, COMSOL Multiphysics software version 5.4 is used for the numerical modeling of the furnace. The software is based on the finite element discretization of the transport equations [18]. The details of the discretization as well as the solver settings for the turbulent flow are described [4]. A linear type of elements are considered for discretizing all transport equations of chemical species as well as radiative transport equation using the finite element method.

The model consists of several physics. In such problems, solving all variables in a single iteration leads to huge memory requirements. The segregated solver in such cases improves the performance significantly. Therefore, a segregated solver approach by defining different segregated steps for relevant groups of variables is used to simulate the model. The segregated solver approach is explained in detail in the previous paper [4]. Table 4 shows the segregated groups that the solver encounters while solving the model. For all segregated groups, the Newton-Raphson method with a constant damping factor is applied to linearize the non-linear transport equation. The Jacobian for the Newton method is updated after every iteration. The corresponding direct/iterative solver for solving the linear equation for each of the segregated step is also mentioned in Table 4.

Table 4
Details of the segregated solver for individual physics.

Segregated step	Variables	Linear solver	Preconditioner
Segregated step 1	u, p	GMRES iterative solver	Algebraic multigrid preconditioner
Segregated step 2	T	Pardiso direct solver	–
Segregated step 3	k, ϵ	GMRES iterative solver	Algebraic multigrid preconditioner
Segregated step 4	w_i	GMRES iterative solver	Algebraic multigrid preconditioner
Segregated step 5	G	Pardiso direct solver	–

Table 5
Summary of models discussed in this paper.

Description	Diffusion tuning parameter	Fuel jet velocity	Fuel pipe diameter
Test case	0	74 m/s	9 mm
Effect of diffusion	0, 0.1, 0.3 & 0.5	74 m/s	9 mm
Effect of fuel jet velocity	0.1	50, 74 & 90 m/s	9 mm
		24 35 & 43 m/s	13 mm
Effect of fuel pipe diameter	0.1	74 m/s	9 mm
		35 m/s	13 mm

Table 6
Values of fuel pipe diameters and velocities that have equivalent mass flow rate.

Fuel mass flow rate [kg/s]	Fuel pipe diameter [mm]	Fuel inlet velocity [m/s]
0.0020	9	50
	13	24
0.0030	9	74
	13	35
0.0037	9	90
	13	43

4. Results and discussion

In this paper, the effect of various operating conditions related to the mixing behavior of air and fuel stream are studied. The test case model is defined by the existing burner design and the operating conditions with the commonly used diffusion parameter settings of the model. The following table (Table 5) provides the summary of all models examined in this section. Note that for all models, the air stream remains unchanged at 0.14 kg/s.

The velocity for the 13 mm diameter fuel pipe model are decided based on the equivalent fuel mass flow rate from 9 mm diameter. Table 6 shows the values of velocities for the two fuel pipe diameters that yields equal mass flow rate of fuel injected in the furnace. As can be expected, for the larger diameter of fuel pipe, the injected fuel inlet velocity is lower.

4.1. Results of the test case model

The test case model is with 9 mm fuel pipe diameter and fuel mass flow rate of 0.003 kg/s. The test case model is the representation existing design from the Aluchemie. The results are compared with the measured values from the furnace. It is important to understand the formation of NO_x with the existing design. Further analysis to reduce the NO_x from the furnace can be extended based on the validated model for the existing design.

The model of the 9 mm pipe diameter is developed systematically in this study. The detailed analysis of the non-isothermal turbulent flow modeling with different meshing techniques is carried out in our previous paper [4]. The results with cfMesh software with the refinement under the fuel outlet provides more accurate results. This model is further improved by adding transport of chemical species, radiation and conjugate heat transfer. In this section, the results of the 9 mm fuel pipe diameter are explained.

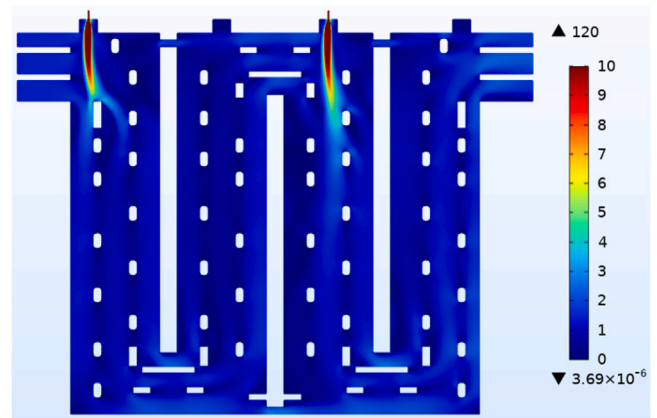


Fig. 4. Velocity magnitude distribution [m/s] in the furnace with 9 mm fuel pipe diameter for fuel mass flow rate of 0.003 kg/s. The momentum of the jet is such that fuel stream is penetrated well within the furnace.

Fig. 4 shows the velocity distribution in the furnace. The inlet velocity for the 9 mm diameter of fuel pipe is 74 m/s. It can be observed that the velocity at the outlet of the fuel pipe is as high as 120 m/s. The high momentum of the jet is responsible for the deeper penetration of jet in the furnace. The velocity of the jet is such that the combustion gases does not flow through the bypass at the top. The higher momentum ensures that the combustion is well distributed in the furnace as explained later.

After developing the initial flow results, the transport of chemical species is included in the model. The turbulent chemistry interaction is modeled by the eddy dissipation model. This model is based on the ‘mixed is burnt’ phenomena. This can be observed from the mass fraction distribution of CH₄ (reactant) and mass fraction distribution of CO₂ (product) as shown in Figs. 5 and 6, respectively. The layer of CH₄ stream that is in contact with the O₂ shows the appearance of the product (CO₂). The reaction zone is limited to the mixing zone of the reactants. This produces sharp gradients of the chemical species throughout the model of the furnace. This result can be attributed to the source term calculated by the eddy dissipation model. The source term of the reaction in eddy dissipation model is strongly related to the turbulence parameters that govern mixing.

Due to the larger penetration of the jet associated with the high momentum, the combustion reaction zone is not limited to the region near the fuel outlet. Moreover, Fig. 5 shows that as compared to the first burner, the traces of CH₄ remain longer in the flame for the second burner. The combustion in the section of the furnace is an example of two staged combustion. Therefore, the air/fuel ratio for the second burner is reduced as compared to the first burner. The stream after the second stage of combustion consists of products from the first stage as well. This causes delayed mixing of the fuel with the oxidizer leaving traces of fuel for longer stream. Moreover, the concentration of CO₂ is higher downstream the second burner. This is the result of mixing of CO₂ formed by the second burner fuel with that of CO₂ formed due to the reaction of fuel from first burner and oxidizer. The overall results provided by the eddy dissipation model follows a streamline and the diffusion is found to be negligible.

The heat energy released by the combustion reaction is modeled using the enthalpy of reaction. The enthalpy of reaction is further calculated based on the stoichiometric coefficient and the enthalpy of formation for the individual species in the reaction. The heat transfer equation is updated by adding the source term of heat of combustion reaction. Fig. 7 shows the temperature distribution in the furnace by adding this source term. It can be observed that the high temperature region in the furnace is coinciding with the combustion reaction zone. Therefore, the temperature follows the streamline where the CO₂ is

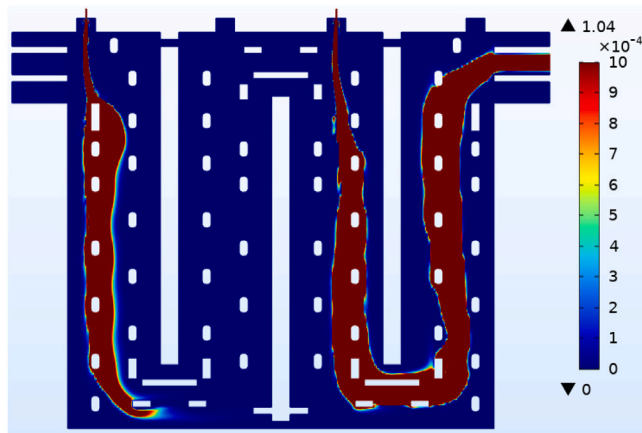


Fig. 5. Mass fraction distribution of CH₄ in the furnace with 9 mm fuel pipe diameter and 0.003 kg/s fuel mass flow rate. The two staged combustion can be observed with incomplete burning of the fuel.

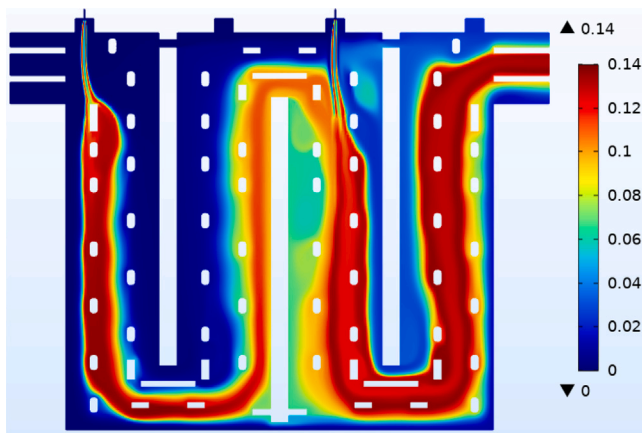


Fig. 6. Mass fraction distribution of CO₂ in the furnace with 9 mm fuel pipe diameter and 0.003 kg/s fuel mass flow rate. The reaction zone is restricted to a narrow stream at both stages.

higher. It can be observed that the central part of the jet is colder than the outer part. This can be attributed to the high momentum of the jet. Due to the momentum, the fuel does not mix with the oxidizer completely. This results in the combustion reaction occurring only at the outside layer. Therefore, the outer part is hotter compared to the central layer of the flame.

The maximum temperature in the furnace is as high as 2470 °C in case of no radiative heat transfer. Moreover, the lower temperature calculated by the model is unrealistic and as low as -11 °C. Therefore, heat transfer by radiation is important phenomena in the anode baking furnace that needs to be incorporated in the modeling. The radiation is modeled by the P1 approximation model. As can be observed from Fig. 8, the temperature distribution becomes more uniform by accounting radiation. The maximum temperature is lowered to 2225 °C due to the heat transfer. The high temperature region is restricted to a layer of combustion reaction zone in the jet.

Another important physical phenomena in the anode baking furnace is the transfer of heat to the anodes. In order to consider the heat flux leaving the gas domain a single brick layer is considered in the model. The temperature measured at the Aluchemie furnace at the brick. Fig. 9 shows the transfer of heat from the fluid domain at the plane passing through both burners.

The temperature calculated from the model is compared against the measured temperature from the furnace. The measurement in the furnace is carried out using an IR thermographic camera (details needed).

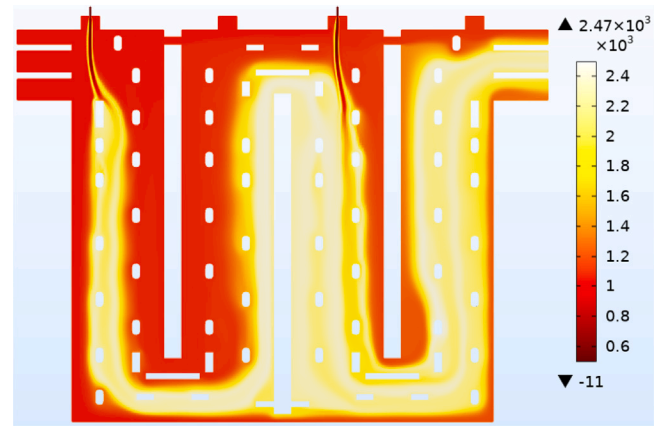


Fig. 7. Temperature distribution [°C] of in the furnace with 9 mm fuel pipe diameter and 0.003 kg/s fuel mass flow rate without considering the radiation. The narrow streamed higher temperatures zones follow from the reaction zones. Temperature at outlet side is higher compared to after the first stage burning.

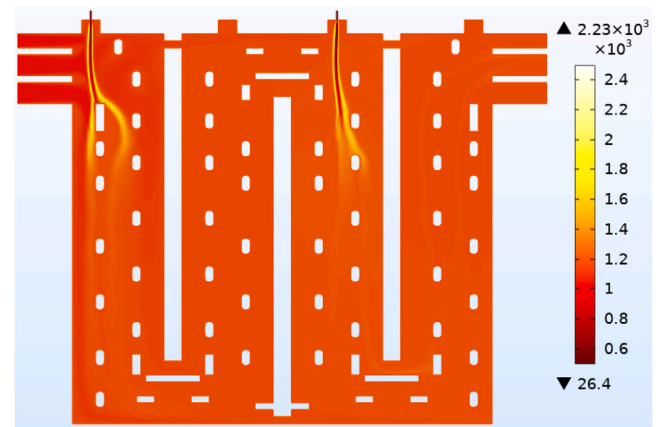


Fig. 8. Temperature distribution [°C] of in the furnace with 9 mm fuel pipe diameter and 0.003 kg/s fuel mass flow rate by considering the radiation. The temperature distribution improves by the addition of radiation along with decreasing the maximum temperature.

Table 7

Comparison of the temperature values from the model and the measurement using IR camera.

Model [degC]	Measurement [degC]	Relative change with respect to the measurement
1208	1204	-0.3%
1209	1281	5.6%

The temperatures from both model and the image of the thermographic camera are extracted at the same plane as shown in Fig. 10. The extracted values are documented in Table 7. It can be observed that the values computed from the model compares well with the measured values. The model values in the plane seems to be more uniform as compared to the measured values. Therefore, at one point of location the difference is as less as 0.08% while at another point the difference is around 6.8%.

The calculated chemical species values from the test case are compared with the measured values. The volume percentage of chemical species such as O₂ and CO₂ are carried out at several locations in the furnace using Testo 350 flue gas analyzer. Fig. 11 shows the location at which the measurements are carried out. The volume percentage of chemical species are extracted at the same locations. Tables 8 and 9 show the comparison of volume percentage calculated with the test

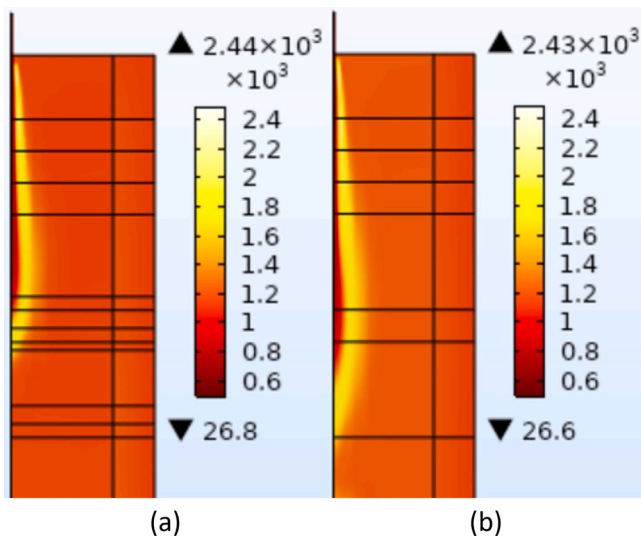


Fig. 9. Temperature distribution [°C] at YZ plane of in the furnace with 9 mm fuel pipe diameter and fuel mass flow rate of 0.003 kg/s passing through (a) first burner and the (b) second burner. The high temperature is restricted to a narrow flame outline. The combustion at the first burner occurs readily as compared to the second burner.

case and the measured values for O_2 and CO_2 , respectively. It can be observed that at Points 1, 2, 4 and 6, the values are comparable. While at Point 3 and 6, there are significant differences. The measured values in a particular region are uniform as opposed to the values from the test case model. The uniformity in the measured values shows that the chemical species are diffusing well in reality at particular region. Furthermore, it can be observed that the O_2 concentration at the outlet, i.e. at points 4, 5 and 6 is lower compared to the measured data. This difference can be explained with the steady state assumption of the model. In reality, the fuel is injected with pulses while the air injection occurs continuously. Therefore, the CH_4 concentration is higher in the model compared to reality. Therefore, more O_2 is consumed in the model to achieve complete combustion. This leads to lower O_2 concentration at the outlet stream from the model.

4.2. Effect of diffusion on transport of chemical species

The results from the test case model motivates to study the effect of different tuning of the diffusion parameter due to the streamline behavior of reaction zone. The effects of diffusion on the transport of chemical species are studied in this section. The diffusion is varied using a tuning parameter as provided in Eq. (11). The diffusion in the

Table 8

Comparison of volume percentage of O_2 calculated by test case model with measurements.

O_2	Test case model [vol%]	Measurement average [vol%]	Difference in the values
Point 1	17.9	17.0	0.9
Point 2	16.4	16.5	-0.1
Point 3	5.72	16.0	-10.2
Point 4	9.34	11.0	-1.6
Point 5	0.57	7.00	-6.4
Point 6	6.90	9.00	-2.1

Table 9

Comparison of volume percentage of CO_2 calculated by test case model with measurements.

CO_2	Test case model [vol%]	Measurement average [vol%]	Difference in the values
Point 1	0.42	2.00	-1.5
Point 2	1.09	2.00	-0.9
Point 3	5.99	3.00	2.9
Point 4	4.37	6.00	-1.6
Point 5	8.26	8.00	-0.2
Point 6	5.47	6.50	-1.0

transport equation increases as the value of the tuning parameter (δ_{id}) approaches a value of unity. The tuning parameter of zero suggests that no such additional isotropic diffusion is added to the transport of chemical species.

Fig. 12 shows the mass fraction of CH_4 for different values of δ_{id} . As can be seen from the figure, the increase in δ_{id} increases the diffusion dominance of the flame. The diffusion parameter also determines the extent of mixing in the furnace. When such additional diffusion is not added ($\delta_{id} = 0$), the lesser mixing causes incomplete reaction in the furnace. This results in the small fraction of CH_4 present in the outlet stream. As the values of δ_{id} increase from 0.1 to 0.5, the spreading of the jet near the burner increases while decreasing the length of the jet. In other words, the diffusive nature of the jet is increasing, while the convective dominance of the jet (as observed in the case of $\delta_{id} = 0$) is decreasing.

The O_2 component of the air stream reacts with CH_4 as soon as it mixes with the fuel stream. The reaction zone is defined as the region in which mixing occurs. Since the extent of mixing is governed by the diffusion parameters, the effect can be analyzed for mass fraction of O_2 and CO_2 as well. Figs. 13 and 14 shows the mass fraction of O_2 and CO_2 , respectively. It can be seen from Fig. 13 that for $\delta_{id} = 0$ the lower values of O_2 are restricted to a streamline. This also means that the reaction zone is confined to this region. In other words, the mixing of two streams is limited to a single stream if additional diffusion is not added. With increasing values of δ_{id} , the mixing of the two streams

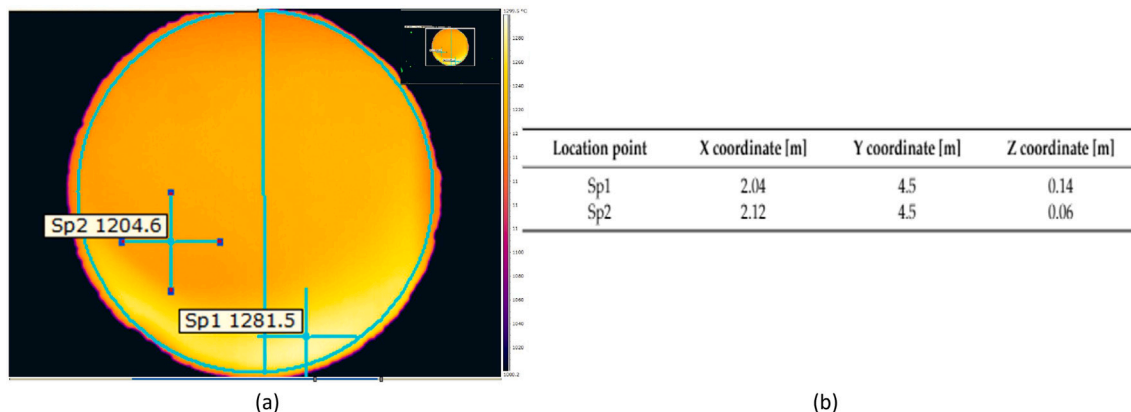


Fig. 10. Location of the temperature computation from (a) measurement from the IR camera and (b) X, Y and Z coordinates of points from the model.

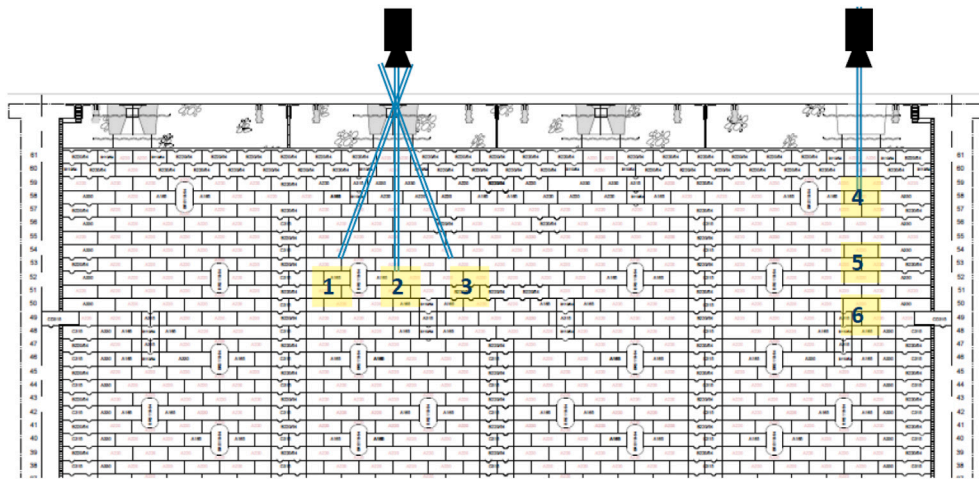


Fig. 11. Location of the measurement points in the furnace. Aluchemie measured volume percentage of chemical species at the given locations. (For interpretation of the references to color in this figure legend, the reader is referred to the web version of this article.)

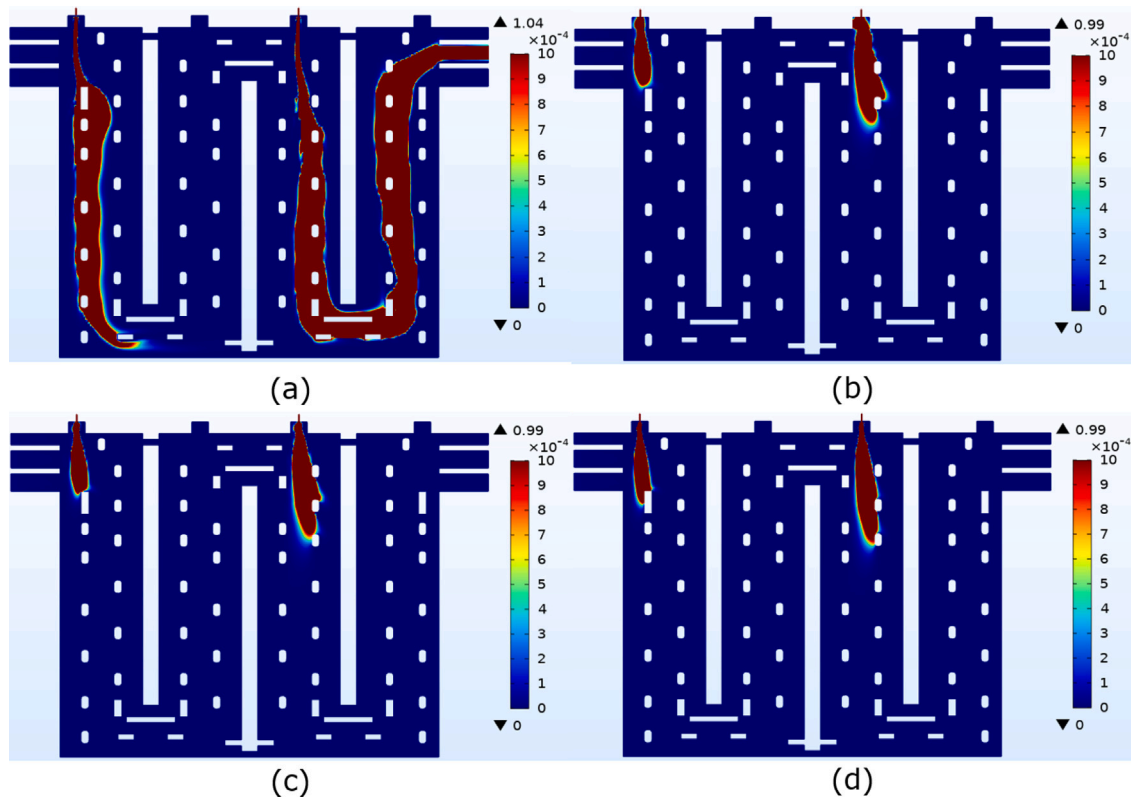


Fig. 12. Mass fraction of CH_4 at XY plane ($Z = 0.27$ m) for (a) $\delta_{id} = 0$, (b) $\delta_{id} = 0.1$, (c) $\delta_{id} = 0.3$ and, (d) $\delta_{id} = 0.5$. The diffusion improves as the tuning parameter increases from 0 to 0.5. Higher diffusion leads to increased mixing which results in faster combustion. This implies negligible CH_4 fraction at the outlet streams for higher tuning parameters.

is spread over a larger region allowing reaction to occur in a wider stream. This spread is accompanied with a lowering of the largest value of mass fraction of O_2 with increasing δ_{id} in the domain of computation. This effect can also be visualized from the mass fraction of CO_2 in Fig. 14. The appearance of CO_2 is limited in the case of no additional diffusion. While the CO_2 is spread out as we increase the diffusion in the transport equations.

The right choice of δ_{id} is required in order to obtain comparable results with the measurements. As discussed in the earlier section, the volume percentage of chemical species such as O_2 and CO_2 are compared with the measured values at the locations shown in Fig. 11.

Tables 10 and 11 shows the volume percentage of O_2 and CO_2 , respectively. The variation of the volume percentage with different values of δ_{id} is compared in these tables. The comparison is carried out by calculating the relative change with respect to the measurement values. The values represented in red color are the values that have less relative change with respect to the measurements for a particular location point. The observation from these tables suggest that the values comparable with measurements are mostly associated with $\delta_{id} = 0.0$ and $\delta_{id} = 0.1$. Furthermore the root-mean-square deviation is calculated for all the location points for a given value of δ_{id} . The lowest value of the root-mean-square deviation for O_2 is when $\delta_{id} = 0.0$. While, the root-mean-square deviation for CO_2 is lowest when $\delta_{id} = 0.1$. For O_2 , the

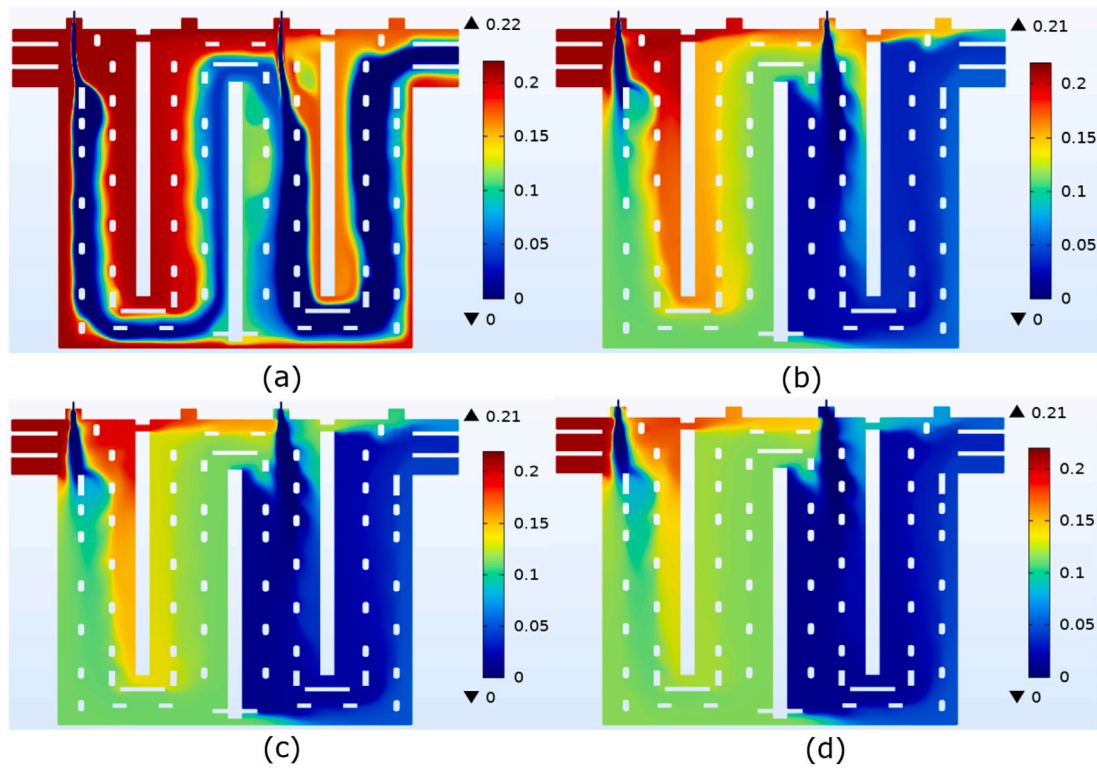


Fig. 13. Mass fraction of O_2 at XY plane ($Z = 0.27$ m) for (a) $\delta_{id} = 0$, (b) $\delta_{id} = 0.1$, (c) $\delta_{id} = 0.3$ and, (d) $\delta_{id} = 0.5$. The diffusion improves as the tuning parameter increases from 0 to 0.5. This leads to wider reaction zones with increase in the tuning parameter. Therefore, the lower mass fraction of O_2 at the outlet is not restricted to a narrow stream for higher tuning parameters as observed from measurements.

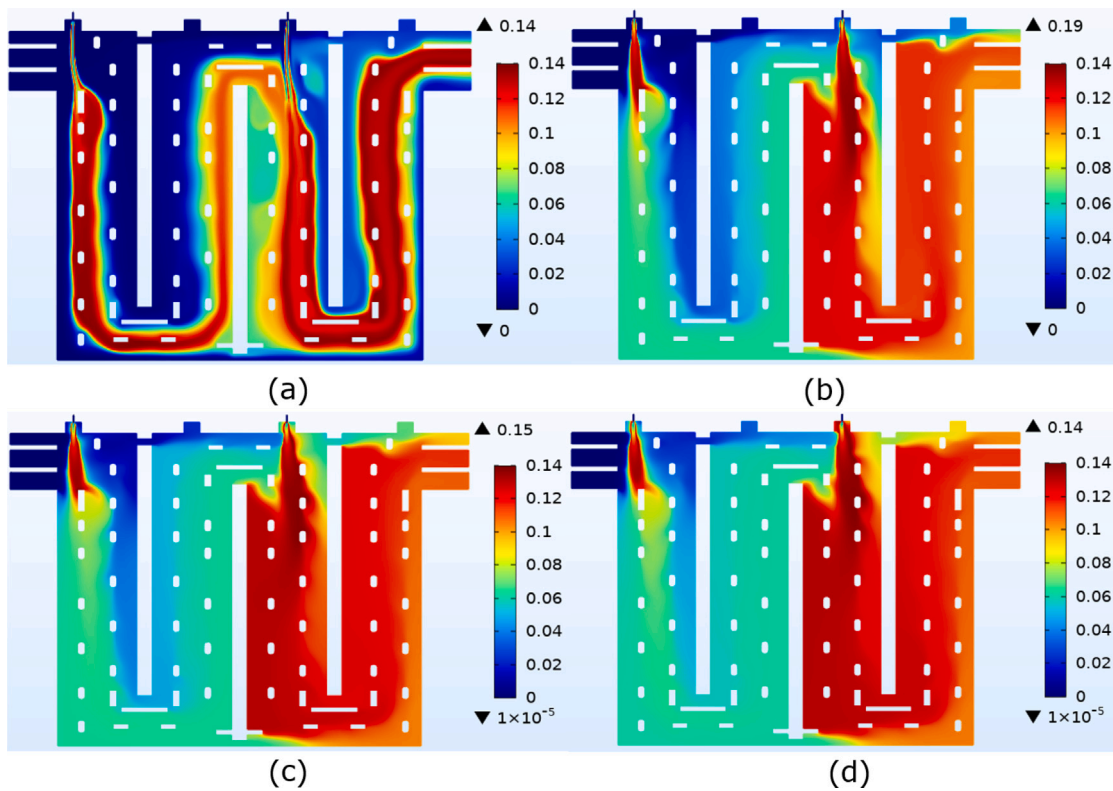


Fig. 14. Mass fraction of CO_2 at XY plane ($Z = 0.27$ m) for (a) $\delta_{id} = 0$, (b) $\delta_{id} = 0.1$, (c) $\delta_{id} = 0.3$ and, (d) $\delta_{id} = 0.5$. The diffusion improves as the tuning parameter increases from 0 to 0.5. This leads to wider reaction zones with increase in the tuning parameter. Therefore, the higher mass fraction of CO_2 at the outlet is not restricted to a narrow stream for higher tuning parameters as observed from measurements.

Table 10
Volume percentage of O₂ for different values of δ_{id} that controls diffusion.

O ₂	$\delta_{id} = 0.0$ [vol%]	$\delta_{id} = 0.1$ [vol%]	$\delta_{id} = 0.3$ [vol%]	$\delta_{id} = 0.5$ [vol%]	Measurement average [vol%]
Point 1	17.9	13.0	11.4	10.6	17.0
Point 2	16.4	11.4	10.6	10.3	16.5
Point 3	5.72	10.2	10.1	10.2	16.0
Point 4	9.34	3.78	3.39	3.16	11.0
Point 5	0.57	3.58	2.97	2.92	7.00
Point 6	6.90	4.51	3.84	3.68	9.00
Relative change with respect to the measurement					
Point 1	0.05	-0.24	-0.33	-0.38	0.00
Point 2	-0.01	-0.31	-0.36	-0.38	0.00
Point 3	-0.64	-0.36	-0.37	-0.36	0.00
Point 4	-0.15	-0.66	-0.69	-0.71	0.00
Point 5	-0.92	-0.49	-0.58	-0.58	0.00
Point 6	-0.23	-0.50	-0.57	-0.59	0.00
Root mean square deviation					
	5.08	5.15	5.79	6.04	0.00

root-mean-square deviation for $\delta_{id} = 0.1$ is slightly higher. Moreover, the measurements suggest that the two chosen regions in the furnace (as shown in Fig. 11) do not show a drastic difference if we vary either the X or Y coordinate. This observation is valid while using additional diffusion. Furthermore, the extent of such diffusion should be limited by a smaller value of δ_{id} . For higher values of δ_{id} , the simulation results vary significantly from the measured values. Therefore, some amount of artificial diffusion is included to obtain a better agreement with the experimental values of O₂ and CO₂ concentrations.

As discussed earlier, the effect of additional diffusion causes more mixing. In this paper, the eddy dissipation model is used for combustion. Therefore, an increase in the mixing of the two streams results in the increase in combustion process. The increase in combustion implies that more reactant is consumed producing more product. This can be validated from the comparisons given in Tables 10 and 11. As we increase the value of δ_{id} (thereby increasing diffusion), the value of O₂ decreases. While, there is an increase in the value of CO₂ at a particular location. Moreover, the comparison of the numerical results of mass fraction of O₂ with the measured data show that the mass fraction of O₂ is underestimated with model for all tuning parameters. As explained earlier, this can be attributed to the steady state assumption of the model. In reality, the fuel is injected in pulses and therefore, the model overestimates the fuel input. Consequently, higher O₂ is required for the combustion resulting into lower values of O₂ as compared to measured data. Furthermore, it is difficult to control the fuel injection mass flow rate in the furnace if the pulsating nature is changed to continuous injection through burner. Therefore, the discrepancy in the results of numerical model and the measured data can be explained. Further, the trials on finding effect of artificial diffusion on the temperature and thermal NOx are carried out. The chemical source term R_i defined by Eqs. (15) and (16), depends non-linearly on the species concentration w_i . Thus, the changes in R_i , temperature and thermal NOx concentration due to changes in w_i and artificial diffusion in the transport equations for w_i are hard to quantify a-priori.

4.3. Effect of variation of fuel velocity

In the earlier section, the variation in the Peclet number is based on the changes in the diffusion coefficient. The decrease in the Peclet number by increasing the diffusion coefficient resulted in increased mixing of fuel and oxidizer stream. In this section the effect of variation on the fuel jet velocity is studied. Fig. 15 shows the mass fraction distribution of CH₄ at the symmetry plane for varying fuel inlet velocities. It can be seen from the figure that for higher velocity, the CH₄ does not readily react with oxidizer in case of 0.0037 kg/s. This can be attributed to the reduced mixing due to higher momentum as well as

Table 11
Volume percentage of CO₂ for different values of δ_{id} that controls diffusion.

CO ₂	$\delta_{id} = 0.0$ [vol%]	$\delta_{id} = 0.1$ [vol%]	$\delta_{id} = 0.3$ [vol%]	$\delta_{id} = 0.5$ [vol%]	Measurement average [vol%]
Point 1	0.42	2.66	3.38	3.74	2.00
Point 2	1.09	3.42	3.76	3.87	2.00
Point 3	5.99	3.94	4.00	3.94	3.00
Point 4	4.37	6.88	7.06	7.17	6.00
Point 5	8.26	6.98	7.25	7.28	8.00
Point 6	5.47	6.55	6.85	6.93	6.50
Relative change with respect to the measurement					
Point 1	-0.79	0.33	0.69	0.87	0.00
Point 2	-0.46	0.71	0.88	0.94	0.00
Point 3	1.00	0.31	0.33	0.31	0.00
Point 4	-0.27	0.15	0.18	0.20	0.00
Point 5	0.03	-0.13	-0.09	-0.09	0.00
Point 6	-0.16	0.01	0.05	0.07	0.00
Root mean square deviation					
	1.63	0.92	1.14	1.25	0.00

the increased quantity of fuel. For a fixed diameter of fuel pipe, the increase in velocity also accounts for the increase in the fuel quantity. For a fixed oxidizer concentration, it takes longer to consume all CH₄. Therefore, the length of CH₄ jet increases with increase in the velocity.

Fig. 16 shows the temperature distribution at the YZ plane cutting through the first burner. As can be seen from the figure, the maximum temperature in the furnace increases with the increase in the velocity of fuel jet. The advection term in the transport equation of the chemical species increases with increase in velocity. In other words, for a given geometry and diffusion rate, the Peclet number increases with increase in the velocity of fuel jet. With this concept, the temperature in the furnace should decrease with the increase in the velocity. However, the increase in the fuel jet also increases the fuel in the furnace. The heating section of the anode baking furnace is always a lean mixture. This means that there is always enough oxidizer for burning. Therefore, the overall combustion in the furnace increases thereby increasing the temperature.

4.4. Effect of increasing the fuel pipe diameter

In the previous section, the increase of velocity resulting into the increase in the amount of fuel in the excess of oxidizer environment is observed. With increasing the velocity, the advection term is also increased. However, in the previous analysis these effects have been suppressed by the predominant effects of increasing the fuel amount. In this section, the effects of advection are studied in such a way that the fuel amount remains the same. This is carried out by increasing the fuel pipe diameter. The diameter of the fuel burner pipe is increased from 9 mm to 13 mm. The velocity of the fuel inlet through the 13 mm fuel pipe is such that the mass flow rate of fuel is equal to that through 9 mm diameter. Earlier in Table 6 the values of velocities for the two fuel pipe diameters that yields equal mass flow rate of fuel injected in the furnace has been listed. The advection term of the flow dynamics with two fuel pipe diameters are different. Moreover, in this comparison the air/fuel ratio for a given mass flow rate of fuel is constant for the two fuel pipe diameters. Therefore, the difference in the results for the two fuel pipe diameters are governed by the difference in the advection.

Fig. 17 shows the velocity profile at the symmetry plane for the mass flow rate of 0.003 kg/s with two fuel pipe diameters. The higher momentum of the 9 mm diameter fuel pipe results in a deeper penetration of the jet in the furnace. The difference in the momentum of the two jets further leads to variation in turbulence. This can be quantified by comparing the turbulent viscosity ratio as shown in Fig. 18. The comparison shows that the turbulent intensity for the 9 mm diameter is higher, especially in the encircled region below the fuel outlet. Due to the higher turbulence produced by the jet of 9 mm diameter, there

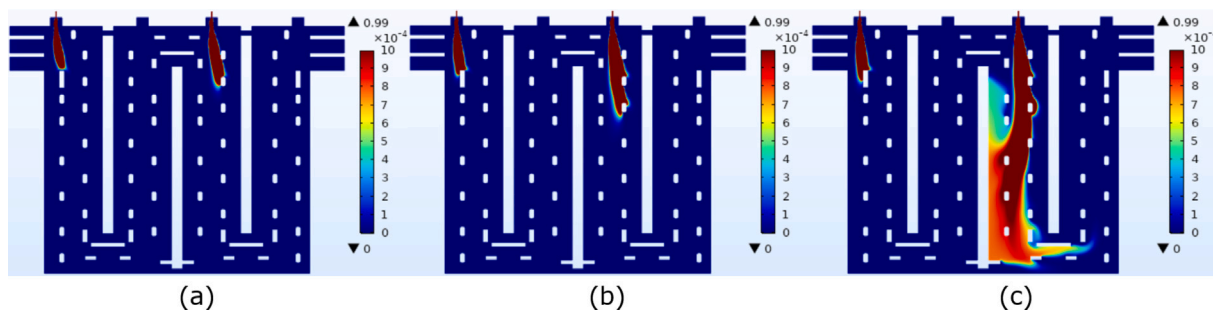


Fig. 15. The CH₄ mass fraction distribution at the symmetry plane for varying fuel inlet mass flow rate of (a) 0.002 kg/s (b) 0.003 kg/s and (c) 0.0037 kg/s with 9 mm fuel pipe diameter. The higher mass flow rate results in the higher momentum of the jet as well as higher amount of CH₄ mass fraction. Therefore, the region of unreacted CH₄ is higher with increased mass flow rate.

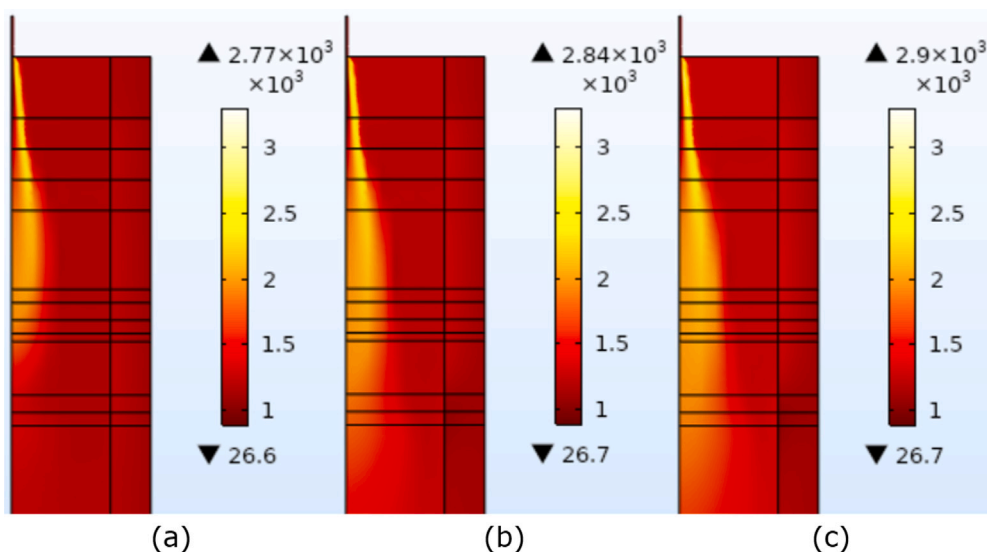


Fig. 16. The temperature distribution (in °C) at the YZ plane through burner 1 for varying fuel inlet mass flow rate of (a) 0.002 kg/s (b) 0.003 kg/s and (c) 0.0037 kg/s with 9 mm fuel pipe diameter. The increased mass flow rate increases the temperature in the furnace due to higher amount of fuel and faster combustion resulting from higher turbulence.

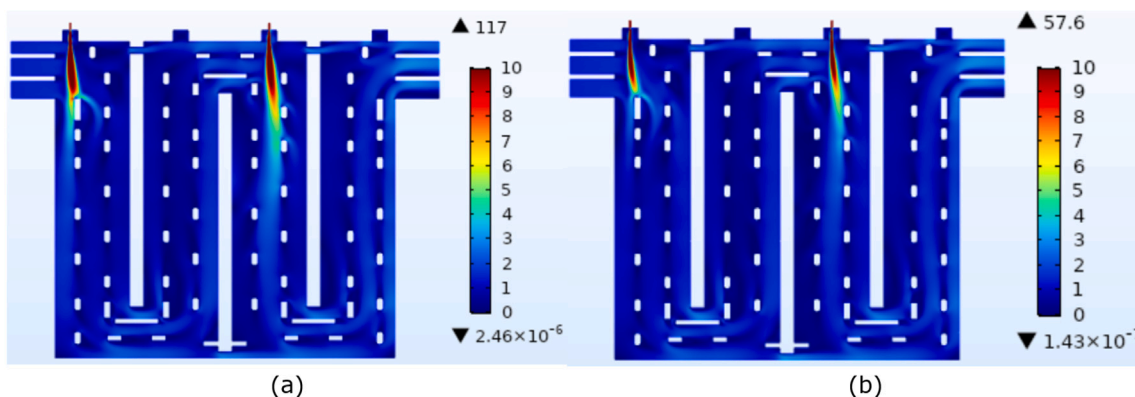


Fig. 17. Velocity magnitude [m/s] comparison at the symmetry plane with the fuel pipe diameter of (a) 9 mm and (b) 13 mm for fuel mass flow rate of 0.003 kg/s. The jet is penetrated deeper for 9 mm fuel pipe diameter due to higher momentum.

is higher mixing of the fuel and oxidizer streams. Therefore, the CH₄ from the fuel jet readily reacts with O₂ from the oxidizer stream.

Fig. 19 shows the mass fraction distribution of CH₄ at the symmetry plane with the two fuel pipe diameters. It can be seen from the comparison that the CH₄ is exhausted by the reaction earlier in case of 9 mm diameter. Whereas, the CH₄ is available till higher depth in case of 13 mm diameter. This aligns with our expectation that due to higher turbulence CH₄ reacts readily with oxidizer in case of 9 mm diameter. This further results in higher temperatures in the furnace for 9 mm fuel

pipe diameter. Fig. 20 (a) and (b) show the temperature distribution at YZ plane passing through burner 1 for 9 mm and 13 mm diameter fuel pipe, respectively. While, Fig. 20 (c) and (d) show the temperature distribution at YZ plane passing through burner 1 for 9 mm and 13 mm diameter fuel pipe, respectively. The maximum temperature with 9 mm fuel diameter pipe is high for both burners 1 and 2 as compared to 13 mm. This is attributed to the higher rate of reaction occurring in accumulated locally in the furnace.

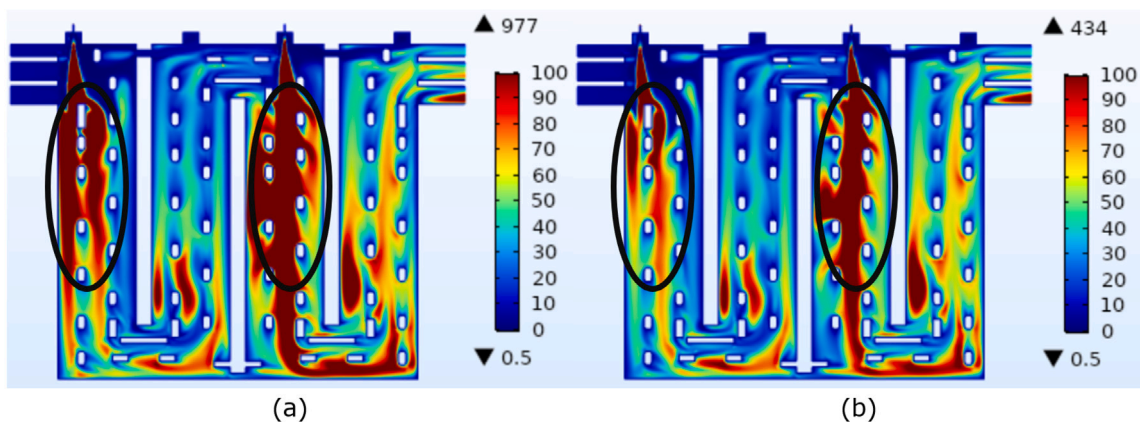


Fig. 18. Comparison of turbulent viscosity ratio at the symmetry plane with the fuel pipe diameter of (a) 9 mm and (b) 13 mm for fuel mass flow rate of 0.003 kg/s. Higher turbulence is observed for the 9 mm fuel pipe diameter due to higher velocity magnitude.

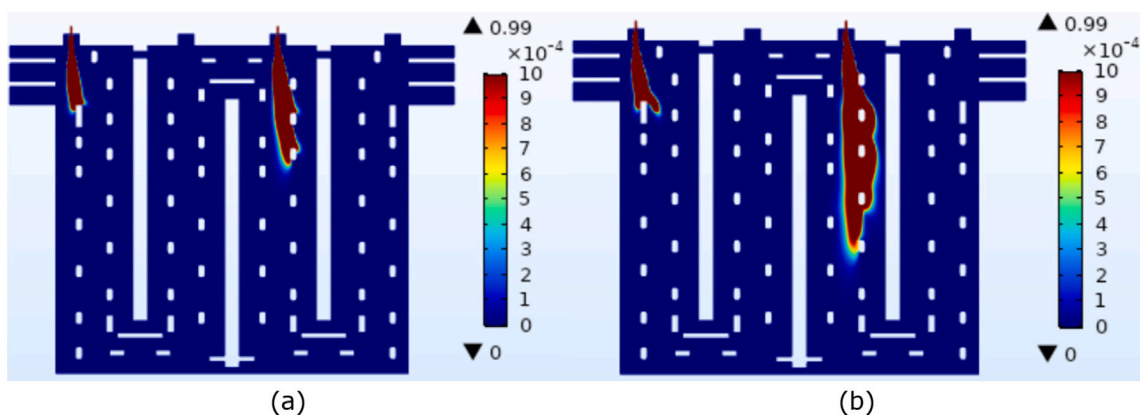


Fig. 19. Comparison of mass fraction of CH₄ at the symmetry plane with the fuel pipe diameter of (a) 9 mm and (b) 13 mm for fuel mass flow rate of 0.003 kg/s. With increased diameter, turbulence decreases due to which combustion process is slower resulting into longer unreacted CH₄ jet.

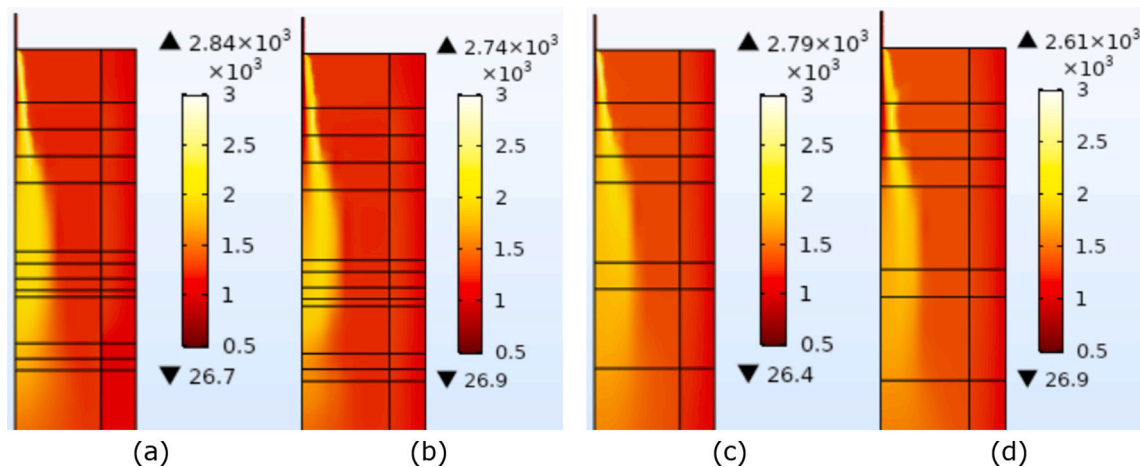


Fig. 20. Comparison of temperature [°C] at the YZ plane with the fuel pipe diameter of (a) 9 mm cutting through burner 1 (b) 13 mm cutting through burner 1 (c) 9 mm cutting through burner 2 and (d) 13 mm cutting through burner 2 for fuel mass flow rate of 0.003 kg/s. Due to increased turbulence with 9 mm fuel pipe diameter, combustion is faster and therefore, temperature is higher compared to 13 mm fuel pipe diameter.

5. Impact on NOx due to varying operating conditions

In the above sections, the effect of varying operating conditions on the mass fraction, temperature and turbulent viscosity ratio across the furnace are compared. The thermal NOx in the furnace depends on the temperature, mass fraction of O₂ and mass fraction of N₂. Therefore, the thermal NOx in the furnace can be computed in post-processing

with the available results. The Zeldovich mechanism as described in the numerical model equations section is used for calculating the NOx.

Before proceeding into discussion on the calculations of NOx, a summary on the impact of fuel pipe diameter and fuel injection velocity is discussed. Fig. 21 shows the temperature at the XY symmetry plane for the studied variations. It can be observed that by increasing the fuel pipe diameter, the maximum temperature in the furnace is

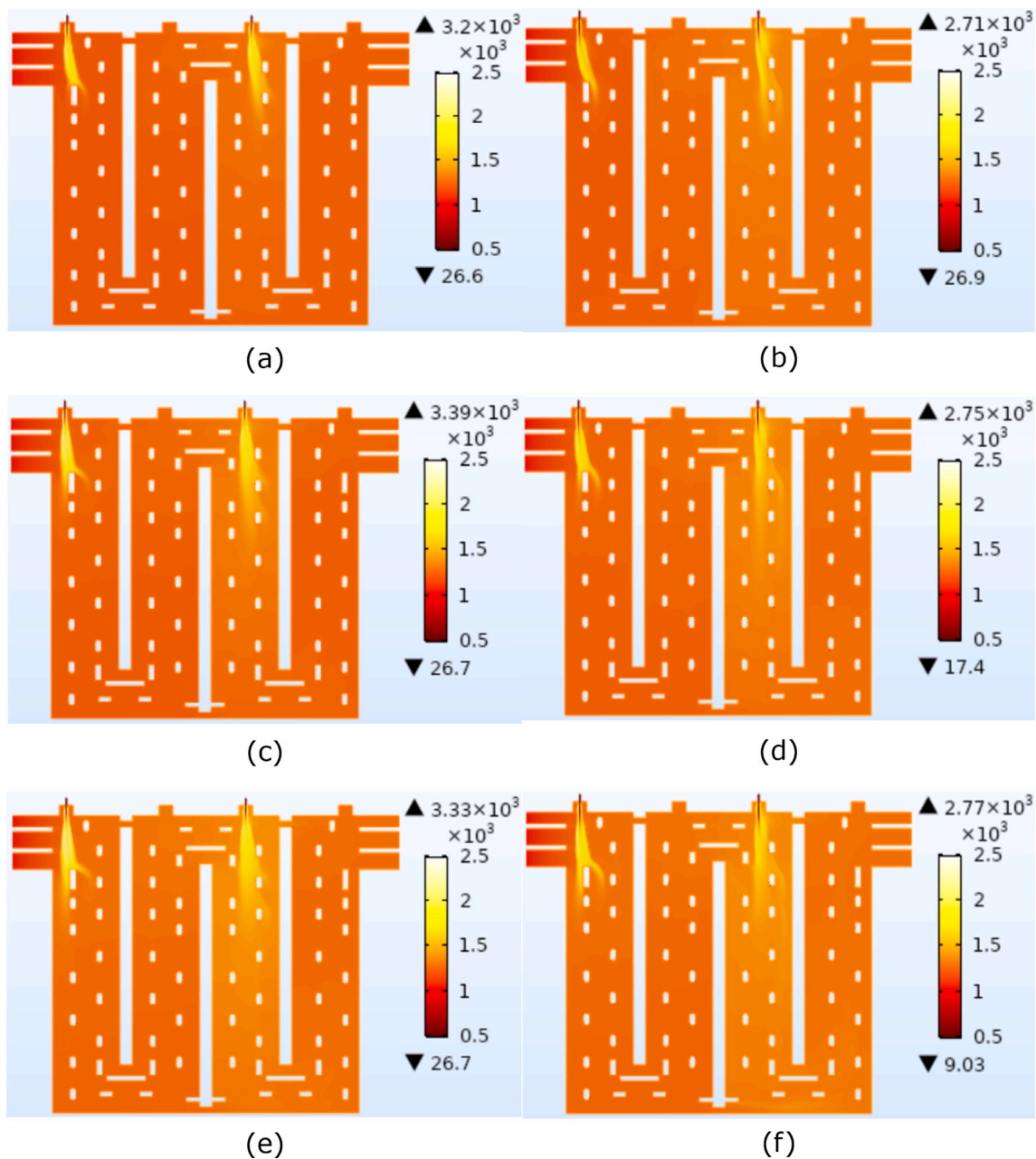


Fig. 21. Temperature [°C] at the XY symmetry plane ($Z = 0.27$ m) with varying fuel pipe diameter and mass flow rate of fuel injection (a) 9 mm and 0.002 kg/s (b) 13 mm and 0.002 kg/s (c) 9 mm and 0.003 kg/s (d) 13 mm and 0.003 kg/s (e) 9 mm and 0.0037 kg/s and (f) 13 mm and 0.0037 kg/s. Temperature decreases with increased fuel pipe diameter. It increases with increased mass flow rate of fuel inlet.

lowered. Furthermore, for a particular diameter, increasing velocity of fuel injection increases the temperature. The reason for the increase in the temperature is closely related to the increased turbulence in the furnace. This can be observed from Fig. 22 that shows the turbulent viscosity ratio across the furnace at the symmetry XY plane. Previously, the authors have validated the finding that the increase in the turbulence intensity increases the heat transfer [19].

Fig. 23 shows that the NO_x at the XY symmetry plane ($Z = 0.27$ m) for varying velocities and fuel pipe diameters. The comparison of Fig. 23 (a) with (b) shows that the overall NO_x is higher in the furnace for the fuel pipe diameter of 9 mm as compared to 13 mm. The same observation can be obtained by comparing Fig. 23 (c) with (d) and Fig. 23 (e) with (f). The effect of increasing velocity for a particular fuel pipe diameter can also be examined. Comparison of results for 9 mm fuel pipe diameter from Fig. 23 (a), (c) and (e) shows that the NO_x generation in the furnace increases for increasing value of fuel jet

velocity. The similar observation can be obtained by comparing Fig. 23 (b), (d) and (f) for 13 mm fuel pipe diameter (see Fig. 23).

The NO_x values are extracted at the same locations represented in Fig. 11 where the measurements are carried out (Fig. 24). The measurement values are available for the current design with 9 mm fuel pipe diameter and operating conditions with mass flow rate of 0.003 kg/s. These values are represented by the black plot. The model values are over-predicted as compared to the measured values. As explained earlier, this over-prediction can be attributed to the steady state assumption in the model as opposed to the reality where fuel is injected in a pulsating manner. Due to the steady state assumption, the model over-predicts the injected fuel resulting into higher combustion. This leads to higher temperature in the furnace causing higher NO_x. However, with the given results, the trends of NO_x can be understood with varying designs and operating conditions. The red and blue colors denote the results of 9 mm and 13 mm diameter fuel pipes, respectively.

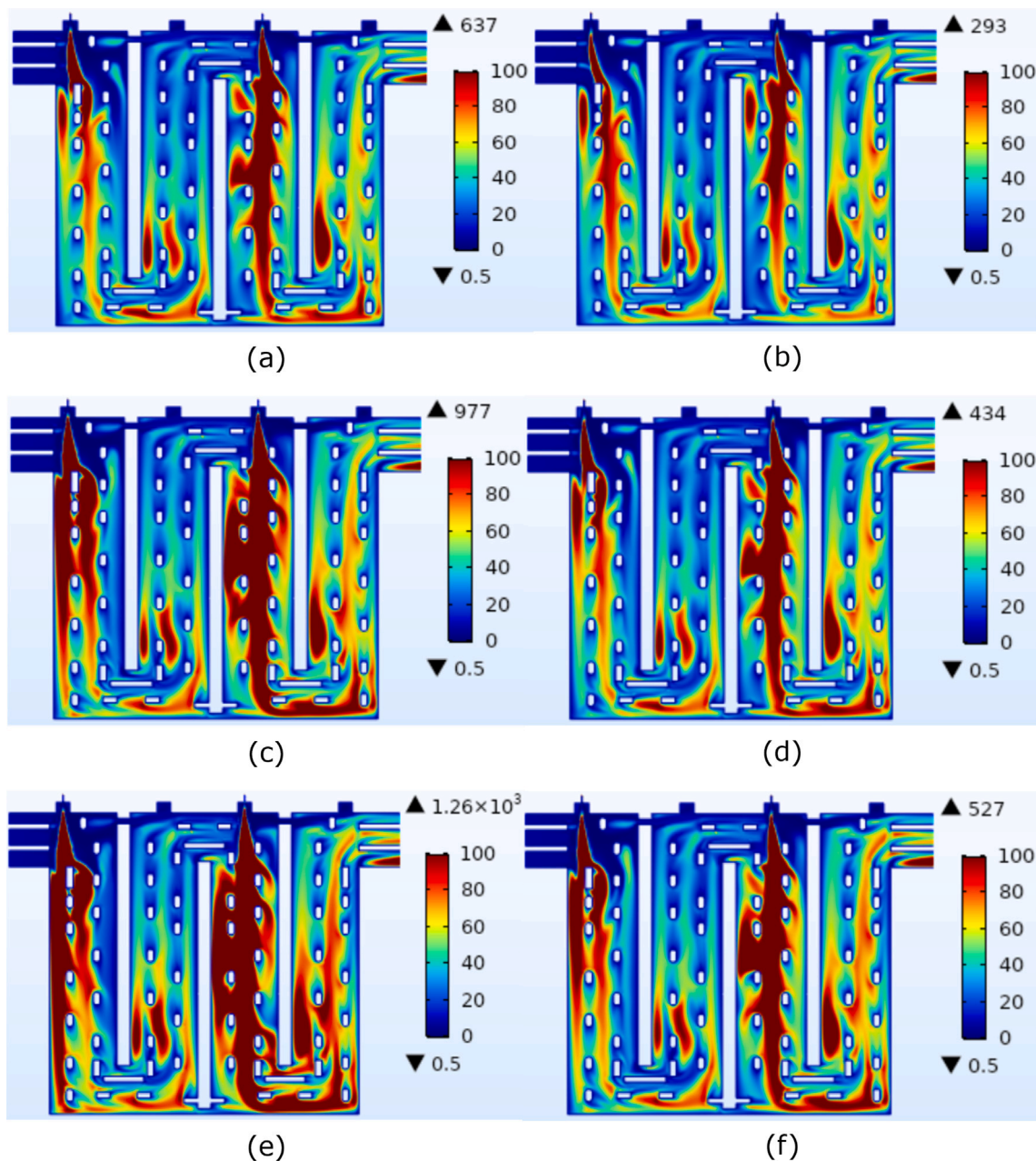


Fig. 22. Turbulent viscosity ratio at the XY symmetry plane ($Z = 0.27$ m) with varying fuel pipe diameter and mass flow rate of fuel injection (a) 9 mm and 0.002 kg/s (b) 13 mm and 0.002 kg/s (c) 9 mm and 0.003 kg/s (d) 13 mm and 0.003 kg/s (e) 9 mm and 0.0037 kg/s and (f) 13 mm and 0.0037 kg/s. Turbulent viscosity ratio decreases with decreased fuel pipe diameter. It increases with increased mass flow rate of fuel inlet.

Moreover, symbols ‘★’, ‘o’ and ‘Δ’ represent values for mass flow rate of 0.003 kg/s, 0.002 kg/s and 0.0037 kg/s, respectively. It can be observed that for a particular symbol, for example ‘★’, the red plots are always higher than the blue plots. This suggests that with increase in the fuel pipe diameter, the NOx across the furnace decreases. Furthermore, for a particular color, for example red, the symbol ‘o’ is always lower than ‘★’ which is further lower than ‘Δ’. This implies that for a given fuel pipe diameter, the NOx decreases with decrease in the fuel pipe diameter.

6. Conclusion

In this paper, a three dimensional model of the heating section of the anode baking furnace is examined to analyze the thermal NOx formation. The COMSOL multi-physics software is used for the modeling of non-premixed turbulent combustion along with the conjugate heat

transfer through lining. In the first part of the paper, the calibration of the model is carried out by comparing temperature and species mass fraction with the measured data from Aluchemie. The test model with tuned diffusion parameter that resembles the existing design and operating conditions provide good comparison with the measured data for the temperature. The O_2 mass fraction is underestimated with the model. However, the trend of O_2 mass fraction through the furnace is well predicted.

The fuel mass flow rate and fuel pipe diameter are varied and their effect on the NOx formation are studied. The motivation for the choice of these parameters is based on their effect on the flow dynamics in the furnace. It can be concluded that by decreasing the fuel mass flow rate from 0.0037 kg/s to 0.002 kg/s for the existing fuel pipe diameter of 9 mm, the NOx decreases by 15%. This decrease can be attributed to the decrease in the turbulent viscosity ratio and fuel amount. The effect of turbulence can further be verified by analyzing the variation

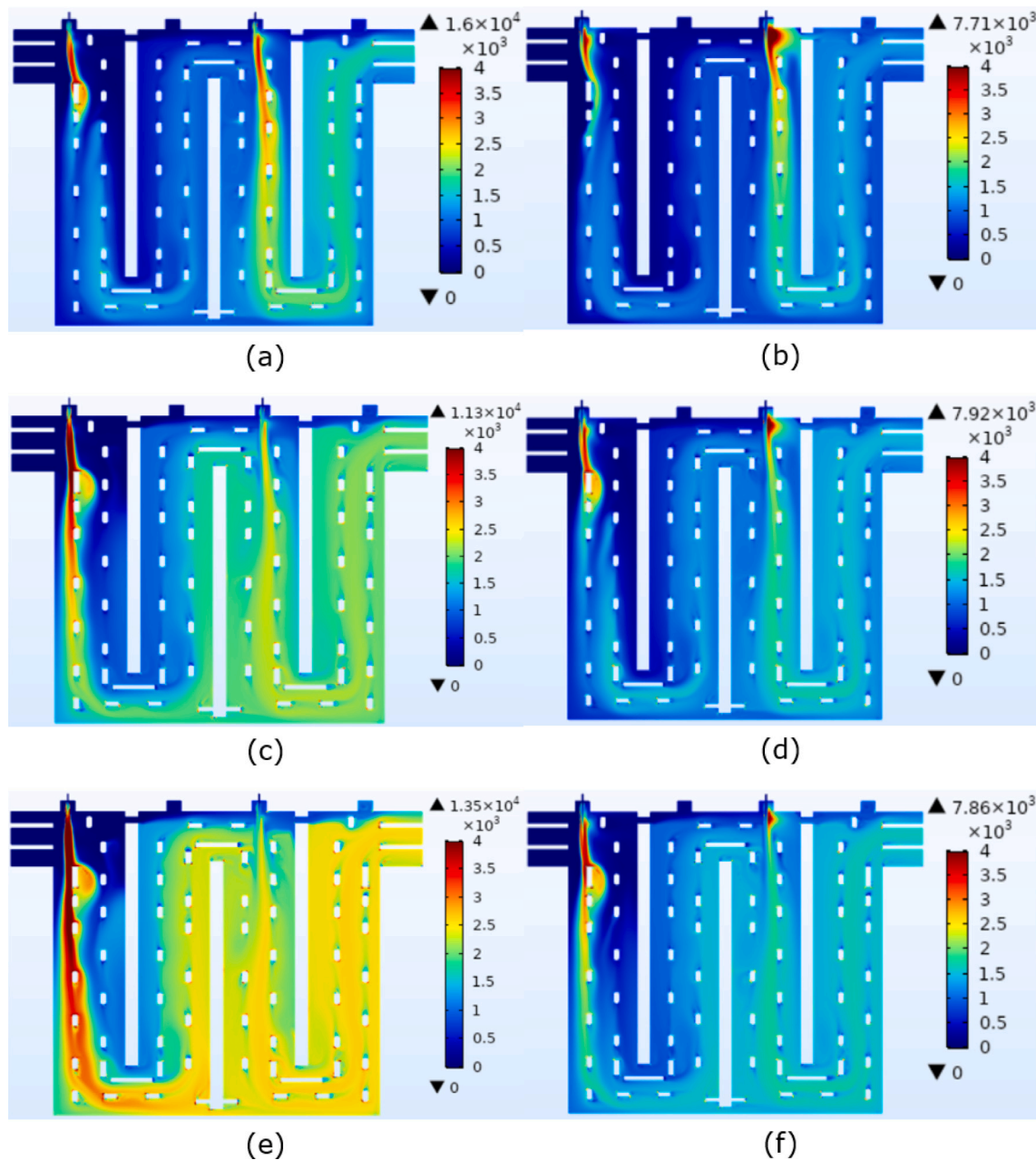


Fig. 23. NOx fraction [ppm] at the XY symmetry plane ($Z = 0.27$ m) with varying fuel pipe diameter and mass flow rate of fuel injection (a) 9 mm and 0.002 kg/s (b) 13 mm and 0.002 kg/s (c) 9 mm and 0.003 kg/s (d) 13 mm and 0.003 kg/s (e) 9 mm and 0.0037 kg/s and (f) 13 mm and 0.0037 kg/s. NOx decreases with decreased fuel pipe diameter. While, it increases with increased mass flow rate of fuel inlet.

in the fuel injection velocity by keeping their mass flow rate constant. This is carried out by varying the fuel pipe diameter. It can be inferred that for an existing fuel mass flow rate in the furnace, the increase in the fuel diameter by 45% decreases the NOx formation by 30% in the furnace. This is due to the decreased turbulence viscosity ratio resulting from the decreased velocity of fuel injection. Though the models from this paper overestimates the NOx formation, they serve the purpose of establishing trends of NOx formation. From the overall comparison of six cases with three fuel mass flow rates and two fuel pipe diameters, it can be concluded that by decreasing the fuel mass flow rate and increasing the fuel pipe diameter by 45%, the peak thermal NOx in the furnace decreases by 42%.

7. Recommendation

The model described in this paper is a multi-physics model comprising turbulent flow, combustion, radiation, and heat transfer to the lining. The sub-models used for modeling these physical phenomena can be improved. It is recommended to consider the detailed chemistry mechanism model. Accounting the detailed chemistry mechanism with the eddy dissipation model provides inaccuracies due to the assumption of equal reaction rates for all reactions. Therefore, combustion models such as the mixture fraction/PDF model are recommended. Further improvement is possible by examining the more precise radiation model such as the discrete ordinate method.

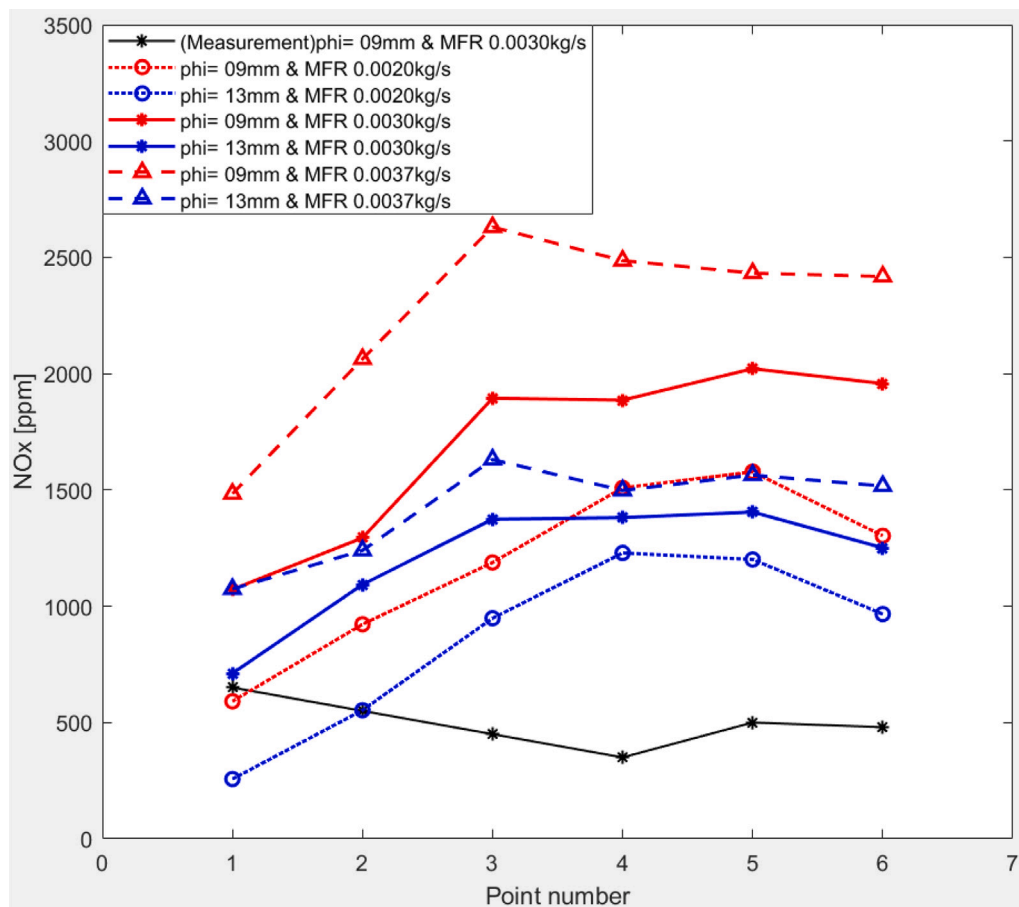


Fig. 24. NOx fraction at six measured point locations for varying fuel pipe diameters and fuel injection velocities. Red and blue colors denote the results of 9 mm and 13 mm diameter fuel pipes, respectively. Black color denotes the measured values for 9 mm diameter and 0.003 kg/s. Symbols ‘*’, ‘o’ and ‘ Δ ’ represent values for mass flow rate of 0.003 kg/s, 0.002 kg/s and 0.0037 kg/s, respectively. NOx calculated from the model are over predicted as compared to measured values. With increased fuel pipe diameter, NOx decreases for a certain mass flow rate of fuel. While, NOx increases with increase mass flow rate of fuel for a certain fuel pipe diameter. (For interpretation of the references to color in this figure legend, the reader is referred to the web version of this article.)

Declaration of competing interest

The authors declare that they have no known competing financial interests or personal relationships that could have appeared to influence the work reported in this paper.

References

- [1] Fluent Ansys, Ansys Fluent Theory Guide, Vol. 15317, ANSYS Inc, USA, 2013, pp. 724–746.
- [2] C.E. Baukal, Industrial combustion pollution and control, in: Environmental Science & Pollution, CRC Press, Boca Raton, FL, USA, ISBN: 9780367578459, 2003.
- [3] Daniel Brough, Jouhara Hussam, The aluminium industry: A review on state-of-the-art technologies, environmental impacts and possibilities for waste heat recovery, *Int. J. Thermofluids* 1 (2020) 100007.
- [4] P. Nakate, D. Lahaye, C. Vuik, M. Talice, Analysis of the aerodynamics in the heating section of an anode baking furnace using non-linear finite element simulations, *Fluids* 6 (2021) 46.
- [5] R.T. Bui, A. Charette, T. Bourgeois, Simulating the process of carbon anode baking used in the aluminum industry, *Metall. Trans. B* 15 (1984) 487–492.
- [6] S. Peter, A. Charette, R.T. Bui, A. Tomsett, V. Potocnik, An extended two-dimensional mathematical model of vertical ring furnaces, *Metall. Trans. B* 27 (1996) 297–304.
- [7] L. Zhang, C. Zheng, M. Xu, Simulating the heat transfer process of horizontal anode baking furnace, *Dev. Chem. Eng. Miner. Process.* (2004) 12.
- [8] D.S. Severo, V. Gusberti, E.C.V. Pinto, Advanced 3D modelling for anode baking furnaces, *Light Methods* (2005) 697–702.
- [9] N. Oumarou, D. Kocaeffe, Y. Kocaeffe, B. Morais, J. Chabot, A dynamic process model for simulating horizontal anode baking furnaces, *Mater. Sci. Technol. Conf. Exhib.* 3 (2013) 2077.
- [10] F. Keller, J.H.M. Disselhorst, Modern anode baking furnace developments, *Essent. Read. Light Methods* (2013) 486–491.
- [11] A.R. Tajik, T. Shamim, M. Zaidani, R.K. Abu Al-Rub, The effects of flue-wall design modifications on combustion and flow characteristics of an aluminum anode baking furnace-CFD modeling, *Appl. Energy* 230 (2018) 207–219.
- [12] M. Zaidani, A.R. Tajik, Z.A. Qureshi, T. Shamim, R.K. Abu Al-Rub, Investigating the flue-wall deformation effects on performance characteristics of an open-top aluminum anode baking furnace, *Appl. Energy* 231 (2018) 1033–1049.
- [13] F. Grégoire, L. Gosselin, Comparison of three combustion models for simulating anode baking furnaces, *Int. J. Therm. Sci.* 129 (2018) 532–544.
- [14] A.R. Tajik, T. Shamim, A.F. Ghoniem, R.K. Abu Al-Rub, The impact of critical operational parameters on the performance of the aluminum anode baking furnace, *J. Energy Resour. Technol. Trans. ASME* 143 (2021) 1–12.
- [15] Mohsen Izadi, Misaghe Abbas Makvand, Ehsanolah Assareh, Farzad Parvaz, Optimizing the design and performance of solid-liquid separators, *Int. J. Thermofluids* 1 (2020) 1000033.
- [16] S.S. Sazhin, E.M. Sazhina, O. Faltsi-Saravelou, P. Wild, The P-1 model for thermal radiation transfer: advantages and limitations, *Fuel* 75 (1996) 289–294.
- [17] Abram S. Dorfman, *Conjugate Problems in Convective Heat Transfer*, CRC Press, 2009.
- [18] J. Donea, A. Huerta, *Finite Element Methods for Flow Problems*, John Wiley & Sons, Hoboken, NJ, USA, 1986.
- [19] Sagar Paneliya, Sakshum Khanna, Umang Patel, Parth Prajapati, Indrajit Mukhopadhyay, Systematic investigation on fluid flow and heat transfer characteristic of a tube equipped with variable pitch twisted tape, *Int. J. Thermofluids* 1 (2020) 100005.